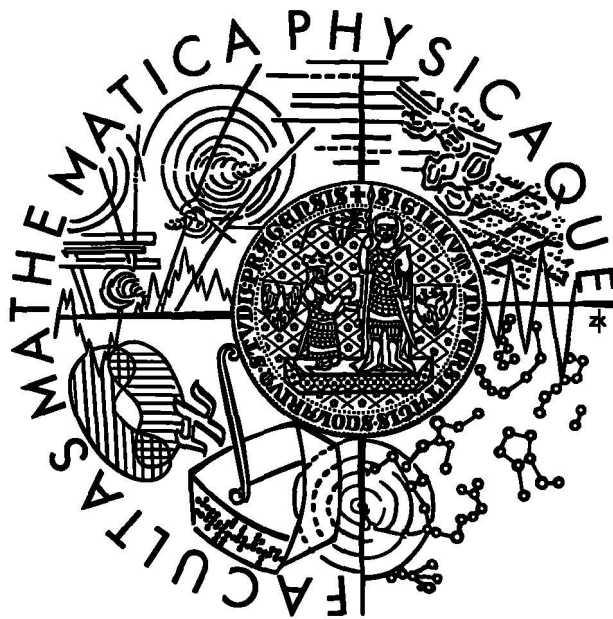Universita Karlova v Praze
Matematicko-Fyzikální fakulta

DIPLOMOVÁ PRÁCE

Richard Polifka

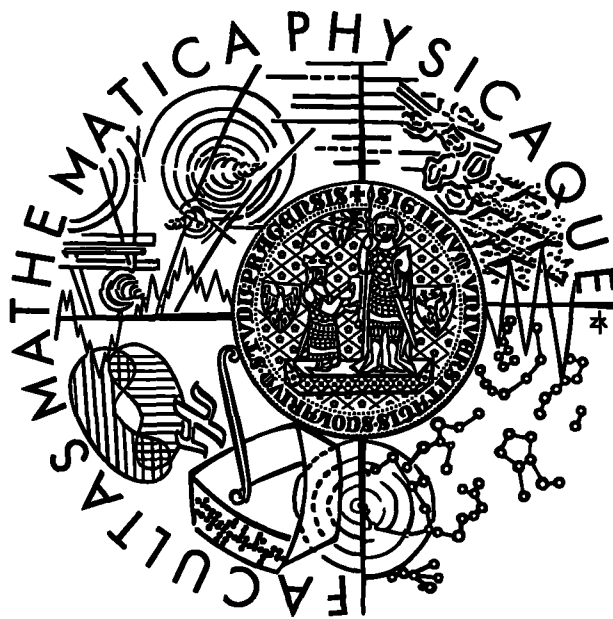# Studium exkluzivní produkce dvou pionů v difrakčních ep interakcích

Ústav částicové a jaderné fyziky

Vedoucí diplomové práce: RNDr. Alice Valkárová, DrSc.
Studijní program: Fyzika, Jaderná a Částicová Fyzika

Charles University in Prague
Faculty of Mathematics and Physics

DOPLOMA THESIS

Richard Polifka

Study of exclusive di-pion production in diffractive ep interactions

Department of Particle and Nuclear Physics

Supervisor: RNDr. Alice Valkárová, DrSc.
Study program: Physics, Nuclear and Particle Physics

Acknowledgements

I would like to thank everyone who lent me a helping hand while I was working on this task.

On the first place, I would like to thank my supervisor, Dr. Alice Valkárová. She supported me from the beginning of my work until the end. She always gave me good advices on her own or she knew whom to ask for help. She also iniciated my admission to the H1 Prague group and later to the H1 community. It was her idea to let me participate on the Diffraction meetings where I got my first experience in presentation of myself and my work.

From the H1 diffraction group, Dr. Hannes Jung deserves my acknowledgements. He introduced me into the problems of theoretical description of diffraction and Xavier Janssen who helped me to solve many problems of technical nature and who gave me his own source code as an inspiration for my work.

At last but not at least I would like to thank Karel Černý for his instant readiness for help.

Rád bych vyjádřil své poděkování všem, kteří mi nabídli svoji pomocnou ruku při vytváření této práce.

V první řadě je to má vedoucí, RNDr. Alice Valkárová, DrSc. Od začátku až do konce nade mnou bděla a pomáhala mi tu radou, tu odkazem na příslušné autority. Dále stála u mého začlenění do Pražské skupiny H1 a do komunity H1. Také se zasloužila o získání mých prvních ostruh na poli přednášení, neboť díky ní jsem měl možnost vystoupit na několika mítincích difrakční skupiny H1.

Z difrakční skupiny bych pak chtěl poděkovat především Dr. Hannesi Jungovi za uvedení do problematiky difrakce po teoretické stránce, Xavieru Janssenovi za mnohé rady technického charakteru a za zapůjčení jeho zdrojového kódu pro moji vlastní inspiraci.

V neposlední řadě bych rád poděkoval Karlovi Černému za jeho obětavou pomoc při mé práci.

Prohlašuji, že jsem svoji diplomovou práci napsal samostatně a výhradně s použitím citovaných pramenů. Souhlasím se zapůjčováním práce.

V Praze dne   Richard Polifka

Abstract

Název práce: Studium exkluzivní produkce dvou pionů v difrakčních ep interakcíc
Autor: Richard Polifka
Katedra (ústav): Ústav částicové a jaderné fyziky
Vedoucí diplomové práce: RNDr. Alice Valkárová, DrSc.
e-mail vedoucího: avalkar@mail.desy.de

Abstrakt: Byla studována produkce nerezonančních dvoupionových eventů na detektoru H1 na urychlovači HERA. Kinematická oblast byla
$4 < Q^2 < 100\ GeV^2$ a energie v γp těžišťovém systému byla v rozmezí
$40 < W < 200\ GeV$. Spektrum invariantních hmot $M_{\pi\pi}$ se nacházelo v oblasti
$1.1 - 3.0\ GeV$. Kromě toho byly hledány další kinematické řezy, aby se minimalizoval vliv rezonancí. Bylo měřeno azimutální rozdělení úhlu svíraného leptonovou a pionovou rovinou v γp systému za účelem srovnání předpovědí dvou teoretických modelů - dvougluonové a pomeronové výměny. Pro srovnání bylo použito Monte Carlo simulované pro oba procesy.

Klíčová slova: nerezonanční piony, difrakční DIS, dvougluonová výměna, pomeronová výměna

Title: Study of exclusive di-pion production in diffractive ep interactions
Author: Richard Polifka
Department: Institute of Particle and Nuclear Physics
Supervisor: RNDr. Alice Valkárová, DrSc.
Supervisor's e-mail address: avalkar@mail.desy.de

Abstract: Production of non resonant di-pion events was studied on the H1 detector at HERA. The kinematical region was $4 < Q^2 < 100\ GeV^2$ and the γp centre-of-mass energy $40 < W < 200\ GeV$. The invariant mass spectrum $M_{\pi\pi}$ was in the range $1.1 - 3.0\ GeV$. Other kinematical cuts have been applied to minimize the influence of resonances. The azimuthal distribution of the pion and lepton plane in the γp frame was measured to compare with the theoretical predictions of the pomeron exchange model and two gluon exchange model. The Monte Carlo for both processes was used for comparison.

Keywords: non resonant pions, diffractive DIS, two gluon exchange, pomeron exchange

Contents

Chapter 1

Theoretical Overview

The main purpose of the HERA accelerator is the study of the structure of the proton. This chapter gives a review of the physics of the lepton-proton collisions. The discussion of the diffractive processes is provided.

1.1 Electron-Proton Scattering at HERA

The idea that hadrons have inner structure was invented in order to explain the wide spectrum of baryons and mesons. The quark model, in which hadrons are composed of spin-$\frac{1}{2}$ constituents (*quarks*) was proposed in 1964 by Gell-Mann [1] and, independently, by Zweig. This model developed out of the SU(3) symmetry (the 'eightfold' way) describing the strong interactions of the baryons and mesons known at the time.

In the Gell-Mann's 1964 model, there were three varieties (*flavours*) of quarks - up, down, and strange. However, the existence of the fourth flavour - charm - was predicted by Glashow, Iliopoulos and Maiani, and confirmed by the discovery in 1974 of the ψ and ψ' mesons. The unexpected discovery of the fifth - bottom - quark led in turn to the expectations of the sixth - the top, the existence of which was confirmed in 1995 by the CDF and D0 collaborations at the Tevatron $p\bar{p}$ collider.

Although quarks were at first thought of as "purely mathematical entities" [1], experiments on inelastic lepton-nucleon scattering from 1968 onwards provided evidence for the existence of a point-like physical objects within the proton and neutron. HERA is the descendant of those early experiments and provides a much more detailed view of the structure of the proton.

1.2 Deep-Inelastic Scattering

The structure of the proton (and neutron) can be investigated using lepton-nucleon scattering. The leptons are point-like (at least up to the resolution of the current measurements) and provide a useful probe of the structure of an extended object such as the proton, the final state being simpler than in a proton-proton collision, where both participating particles are extended objects.

The electron[1] interacts with the proton or one of the constituents of the proton by exchange of an electroweak vector boson - a photon or Z^0 in the neutral-current process $ep \rightarrow eX$, or a $W^{\pm}$ in the charged-current process $ep \rightarrow \nu X$. Fig.1.1(a) is a schematic diagram of an ep collision. The inclusive neutral- or charged-current process can be characterized by following kinematic quantities:

$$s = (k+p)^2 \tag{1.1}$$

$$Q^2 = -q^2 = -(k-k')^2 \tag{1.2}$$

$$x = \frac{Q^2}{2p \cdot q} \tag{1.3}$$

$$W^2 = (p+q)^2 \tag{1.4}$$

$$\nu = \frac{q \cdot p}{m_p} \tag{1.5}$$

$$y = \frac{q \cdot p}{k \cdot p} \tag{1.6}$$

These have the following interpretations:

- s is the square of the centre-of-mass energy of the ep system

- Q^2 is the virtuality of the exchanged boson and determines the length scale $\lambda \sim \frac{1}{\sqrt{Q^2}}$ at which the proton is probed

- x is a dimensionless variable, its interpretation in the quark-parton model will be mentioned later

- W is the centre-of-mass energy of the boson-proton system

- ν is the energy of the boson in the rest frame of the proton

- y is the fraction of the electron's energy carried by the boson in the rest frame of the proton

---

[1]In this thesis, references to the beam lepton as *electrons* apply also to positrons, except where otherwise stated
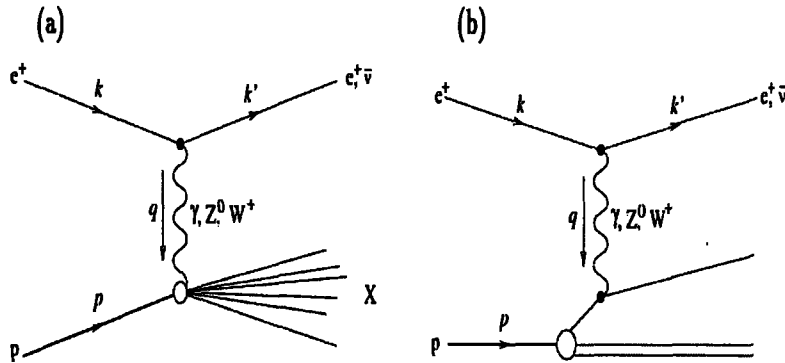
Figure 1.1: A schematic diagram of a deep-inelastic ep interaction (a) in general and (b) in the quark-parton model. The labelled arrows indicate the four-momenta of the particles

The exchange of a vector boson of mass M introduces a propagator of the form

$$\frac{1}{Q^2 + M^2} \tag{1.7}$$

into the scattering amplitude. Thus the cross section for ep scattering is dominated by low-Q^2 photon exchange. The heavier Z^0 and $W^\pm$ only make a significant contribution when Q^2 is around M_W^2 or larger, and charged-current interactions form only a small part of the total cross section.

When the virtuality Q^2 of the exchanged boson is large compared to m_p^2, the proton is probed at a small scale, the boson interacts with one of the proton constituents rather than with the whole proton itself. Such process is called $deep - inelastic\ scattering\ (DIS)$.

Using the single-photon approximation, in which contributions from multiple photon exchange are neglected, the cross section for inclusive neutral-current DIS process (summed over all final states) may be expressed as

$$\frac{d^2\sigma_{ep\to eX}}{dxdQ^2} = \frac{4\pi\alpha_{em}^2}{xQ^4}\left[xy^2F_1(x,Q^2) + (1-y)F_2(x,Q^2)\right] \tag{1.8}$$

where F_1 and F_2 are known as the $structure\ functions$ of the proton. For spin-$\frac{1}{2}$ partons, the contribution from the exchange of longitudinally polarised photons is zero, and F_1 and F_2 are connected by the $Callan - Gross$ relation

$$2xF_1 = F_2, \tag{1.9}$$

which is supported fairly well by the data. Because the structure functions describe the inclusive process, they can be measured even if only the scattered lepton is detected, and not the hadronic final state. Although structure functions say nothing about the nature of the final state, they nevertheless provide a lot of information about the structure of the nucleon.

Experiments using lepton beams to measure the nucleon structure functions in DIS were first carried out in 1968 at SLAC [2] and DESY [3]. These both experiments as well as many others used lepton beams and some material with low proton number Z as fixed targets. A much larger centre-of-mass energy is made possible by a colliding-beam experiment and HERA has been built with the purpose to measure the structure function F_2 over an extended range in x and Q^2.

1.2.1 The Quark-Parton Model

It is found that the structure function F_2 is fairly insensitive to the scale Q^2 [4] indicating that the photon is scattering on point-like objects. This scaling independence is known as *Bjorken scaling*. The experimental support for the Callan-Gross relation (1.9) implies that these *partons* have a spin of $\frac{1}{2}$. In the *quark − parton model* (QPM) [5], proposed by Feynman, they are identified with the quarks postulated by Gell-Mann and Zweig. When probed by a highly virtual photon, the quarks behave like free objects, and DIS may be treated as the elastic scattering off quarks. In fact, quarks are never observed in their free state, but only as bound compound objects (hadrons) made of quarks and anti-quarks (e.g. $qqq,q\bar{q}$ states). However, the hadronization process, whereby the struck quark and the proton remnant in a DIS event form the observed hadronic final state, takes place over a longer time and may be considered as independent of the underlying eq interaction. According to this model, as long as the mass of the quark can be neglected, the Bjorken x may be interpreted as the fraction of the proton's momentum carried by the struck quark in an infinite proton momentum frame.

The quark parton model relates the nucleon structure function F_2 straightforwardly to the momentum distribution of the nucleon's constituent quarks:

$$F_2(x) = \sum_q e_q^2 x f_q(x) \qquad (1.10)$$

where the sum is over the quark flavours, e_q is the charge of the quark flavour q and $f_2(x)dx$ is the expected number of quarks of flavour q carrying the fraction of the protons momentum between $x + dx$. Because the quarks are assumed to be point-like, eq. (1.10) has no dependence on the scale Q^2. Using (1.10) and the experimental results for the structure functions F_2^p and F_2^n of the proton
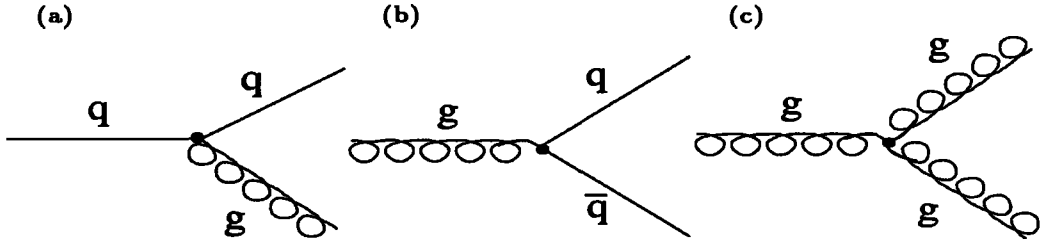
Figure 1.2: Some processes involved in the evolution of partons to small x in QCD

and neutron and assuming the quark model of the proton resp. neutron uud, resp. udd, the average momentum fraction x carried by each quark flavour can be calculated. It is found that the quarks only account for a total of about half of the momentum of the proton:

$$\sum_x \langle x \rangle = \sum_q \int_0^1 x f_q(x) dx = \frac{9}{5} \int_0^1 \left[F_2^p(x) + F_2^n(x) \right] dx \approx 0.5. \qquad (1.11)$$

1.2.2 Quantum Chromodynamics

If the parton is to make sense, the rest of the momentum of the proton must be carried by neutral constituents, which do not couple to the photon and are therefore invisible to DIS. This puzzle was solved in 1970s by the introduction of *quantum chromodynamics*(QCD), the theory of the strong interaction between quarks. The strong force is carried by gluon - neutral vector bosons that carry the "missing" half of the momentum of the proton. Another problem with the simple quark-parton model is the fact that the scale-invariance of F_2 is only approximate: at small values of x,F_2 increases with Q^2, while at large x it decreases. This is explained by QCD, too. As Q^2 increases, the proton is probed at a smaller scale, and the radiation of gluons by quarks becomes important as well as the splitting of gluons into a $q\bar{q}$ and gg pairs (see Fig. 1.2). This means that at large Q^2 a large population of low-momentum (small-x) partons is seen, while the large-x valence quarks loose momentum by radiating gluons. This shift towards small x explains why F_2 falls at large and grows at small x. The QCD-based DGLAP equations [6] provide a successful description of the way F_2 evolves with increasing Q^2.

The fact, that gluons themselves carry colour (the charge associated with the strong force) and can thus exchange further gluons with an other, leads to running of the strong coupling parameter α_s in the opposite direction to that of the electromagnetic coupling α_{em}. At large momentum transfers (short distances),

α_s is strong and the interaction is relatively weak. This has the consequence that quarks probed with a high-Q^2 photon behave as if they were not influenced by the other partons in the proton. This behaviour, *asymptotic freedom*, is responsible for the success of the simple quark-parton model. At small momentum transfers (long distances), the α_s is large. In fact it is so large that the energy required to separate a quark from the proton remnant is larger than that required to produce a new quark-anti-quark pair. Thus the space between the struck quark and the proton remnant is populated with hadrons, but an individual, free quark is never produced. This *confinement* is the reason that only colourless states are ever observed.

Where the relevant momentum scale is large enough (larger than about 1 GeV^2) that α_s is much less than unity, perturbation theory may be used to predict cross sections from QCD. When no such "hard scale" is present, perturbation theory is not applicable and there is no way of making precise predictions. Instead, various phenomenological methods are used.
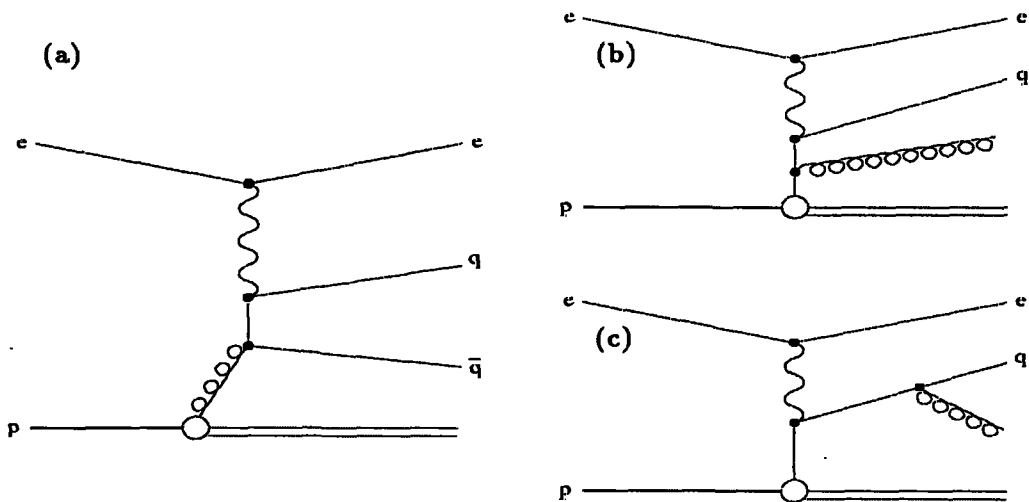
Figure 1.3: Higher-order QCD contributions to ep scattering: (a) BGF, (b) and (c) QCDC

The simple quark-parton model diagram in Fig. 1.1 is supplemented in QCD by high-order processes such as boson-gluon fusion (BGF) and QCD Compton radiation (QCDC), as illustrated in Fig 1.3. In these processes, the system produced by the proton-parton interaction cannot be treated as massless and the Bjorken variable x is no longer simply the momentum fraction carried by the struck quark.

1.3 Diffractive Scattering and the Pomeron

Events with a large rapidity gap - a region free of hadrons between the proton remnant and the current region - have been observed both in photoproduction [7] and in DIS [8] at HERA. Such events are being explained as due to the exchange of a colourless object, so there is no string of Colo field connecting the two parts of the hadronic final state and filling the gap by hadronization. Similar "diffractive" events have been observed for decades in hadron-hadron collisions, but there is no agreed mechanism for them in terms of QCD. They are, however, well described by the Regge theory the phenomenological model of colourless exchanges between hadrons, which predates QCD. DIS at HERA offers a new way of probing the partonic structure of the diffractive exchange and thus distinguishing between the various models that have been proposed.

This section begins with a discussion of hadron-hadron interactions and their description in terms of Regge theory. Then the connection with lepton-hadron interactions is explored, along with the ways in which diffractive interactions are investigated at HERA, and some of the models are described.

1.3.1 Hadron-Hadron Interactions

Cross sections for hadron-hadron scattering contain a large contribution from elastic processes with a small four-momentum transfer. These are soft interactions, the relevant value of the coupling α_s is too large for perturbative QCD to be used. The best description of such processes is still provided by pre-QCD phenomenological models based on general considerations such as crossing symmetry and the analycity of scattering amplitudes.

At high energies, scattering amplitudes are dominated by exchange terms, which vary smoothly with energy, free of the resonance structure which dominates at lower energies. The objects exchanged in elastic interactions (and in all long-range interactions, due to colour confinement) are colour singlets. Crossing symmetry is used to relate the exchange of these states in the t-channel reaction to the formation of the same state as a resonance in the corresponding s-channel reaction (see Fig. 1.4.). The scattering amplitude for the t-channel process is obtained by analytically continuing the amplitude for the s-channel into a different region of s and t.

The simplest approach is to consider only the exchange of the lightest meson consistent with conservation of relevant quantum numbers. This is the $one-particle\ exchange$ (OPE) model. The exchange brings a propagator of the form
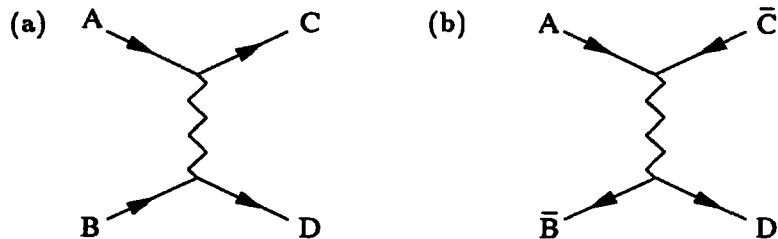
$$\frac{1}{m^2 - t} \tag{1.12}$$

10

Figure 1.4: An illustration of the relationship between (a) the t-channel reaction $AB \to CD$ and (b) the corresponding s-channel reaction $A\bar{C} \to \bar{B}D$.

into the scattering amplitude, where m is the on-shell mass of the exchanged particle and t is the square of the four momentum transfer. Since t is negative, the largest contribution comes from the lightest possible exchanged particle. Thus the OPE model provides a reasonable description in cases where exchange of one particle dominates. In 1935 Yukawa used this model, in conjunction with measurements of the range of the force between nucleons, to predict the existence of the π^0 meson. However, for a more accurate and general description of cross sections for hadronic scattering, it is necessary to take into account all contributing exchanges.

Experiments on the scattering of pion beams by hydrogen targets revealed patterns in the resonances produced. When the spin of each resonance (or bound state) is plotted against the square of its mass, resonances with identical quantum numbers (other than spin) are found to lie approximately on straight lines, called *Regge trajectories* (see Fig. 1.5). This behaviour can be rationalised for mesons using a simple QCD-inspired model in which a meson consists of a quark and an anti-quark connected by a string of gluons with energy proportional to its length. In such a system, the angular momentum of the meson is proportional to the square of the total energy.

Regge theory [9] is used to add up the contributions from all mesons on a trajectory. The straight line $\alpha(m^2)$ relating the spin α of each particle to its mass m is relabelled

$$\alpha(t) = \alpha(0) + \alpha' t \qquad (1.13)$$

where t, the four-momentum squared, is equal to the mass of a meson where t is positive and α is an integer, and to the squared four-momentum transfer in an exchange where t is negative. The contributions are added up using a method in which angular momentum is treated as a complex quantity, resulting in a scattering amplitude
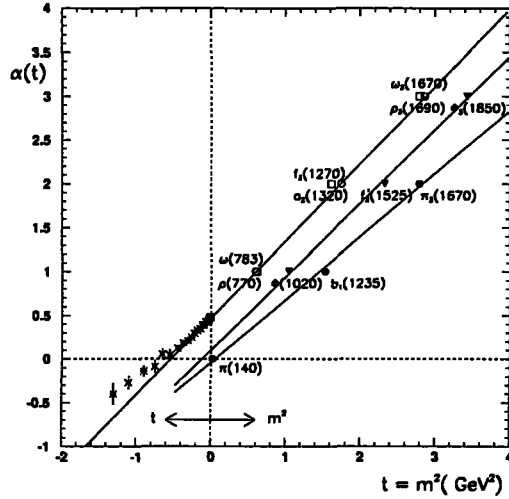
Figure 1.5: Chew-Frautschi plot: Spin J versus m^2 for different mesons

$$A(s,t) \sim f(t) \left(\frac{s}{s_0}\right)^{\alpha(t)} \tag{1.14}$$

and a differential cross section for the two-body process $AB \to CD$

$$\frac{d\sigma}{dt} = F(t) \left(\frac{s}{s_0}\right)^{2\alpha(t)-2}. \tag{1.15}$$

The total cross section for AB interactions is related by the optical theorem to the imaginary part of the forward ($t = 0$) amplitude for elastic AB scattering. Using the Regge scattering amplitude, it is found to be

$$\sigma_{tot}(AB) \sim \left(\frac{s}{s_0}\right)^{\alpha(0)-1} \tag{1.16}$$

The exchange of such set of trajectories is called the *Reggeon* exchange and the diagram is schematically shown on Fig. 1.6.

All trajectories have intercepts $\alpha(0)$ less than 0.6. If these mesons were the only exchanged objects responsible for the behaviour of hadronic scattering, the elastic and total energy would decrease with increasing centre-of-mass energy $\sqrt{s}$. This is indeed the case at low energy ($\sqrt{s} < 10 \; GeV$), but at high energy a slow increase is seen as on Fig. 1.7. This corresponds to exchange of a trajectory with an intercept $\alpha(0)$ greater than one, matching none of the known mesons, and in the Regge picture is identified with the exchange of objects carrying even
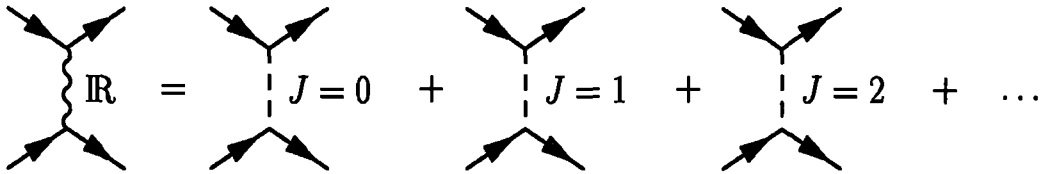
12

Figure 1.6: The Reggeon trajectory is equivalent to sum of many particles with different spins

spin and the quantum numbers of vacuum. This is the *vacuum* or *Pomeranchuk* trajectory, also known as the *pomeron*($I\!P$). Scattering processes involving the exchange of the quantum numbers are termed *diffractive*, because the shape of the differential cross section plotted against t resembles the diffraction pattern seen when a coherent beam of light is obstructed by a small obstacle. Diffractive processes include not only elastic scattering, but also processes in which one or both of the of the incoming hadrons are excited into a higher-mass state and break up. This is *diffractive dissociation*.

The positive slope of the α' of the Regge trajectories means that the dependence of the elastic cross section on t becomes steeper as the centre-of-mass energy of the reaction is increased. In other words, the forward diffractive peak becomes narrower. This phenomenon is called *shrinkage* and has been observed in hadron-hadron interactions.

As the pomeron has the quantum numbers of the vacuum, it is expected to couple equally to any particle and to its antiparticle. Thus the ratio of the elastic pp and $p\bar{p}$ cross section should be equal to unity at high enough energies, where pomeron exchange dominates, and a similar result holds for the total cross sections. This result is given by the *Pomeranchuk theorem* [10] and is borne out by the data.

Donnachie and Landshoff [11] have fitted total cross section for a variety of hadronic interactions using the Reggeon contribution (dominates at low energy), and the Pomeron contribution (dominates at high energy), assuming an universal pomeron:

$$\sigma_{tot} = X s^{\alpha_{I\!P}(0)-1} + Y s^{\alpha_R(0)-1} \tag{1.17}$$

They found a good agreement with the experimental results and obtained a value of $\alpha(0) = 1.0808$ for the pomeron intercept and $\alpha(0) = 0.5$ for the reggeon intercept. They also note that the cross sections for πp and pp scattering are in a ratio about 2:3, hinting that the pomeron may obey an *additive quark rule*,
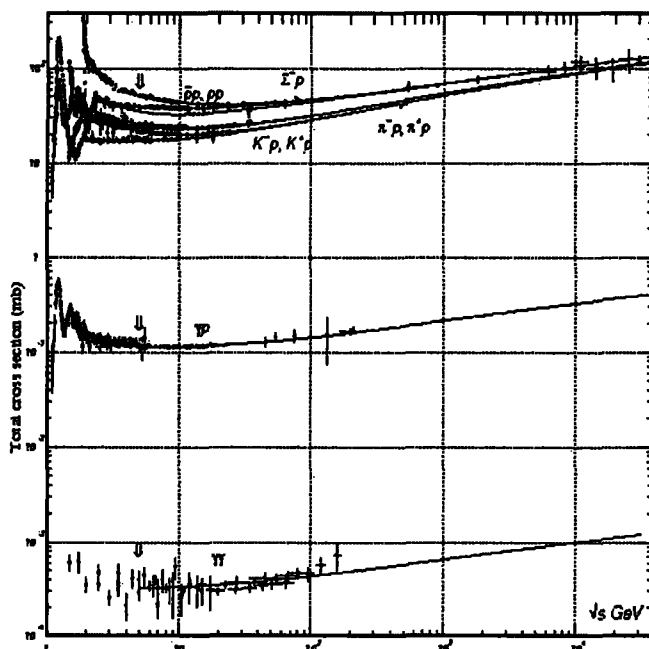
13

Figure 1.7: The increase of the σ_{tot} with the $\sqrt{s}$

coupling to individual valence quarks rather than to the hadron as a whole.

It is still not clear what the pomeron *is* in terms of QCD, despite the success in describing the hadron-hadron scattering. The simplest relevant QCD process is exchange of a pair of gluons and it has been suggested the Pomeranchuk trajectory is a line linking glueball states. A resonance with the right quantum numbers ($J^{PC} = 2^{++}$), showing evidence of a significant gluon content, has been seen at a mass of 1900 MeV by the WA91 and WA102 collaborations [12, 13].

Ingelman and Schlein [14], treating the pomeron as an object with a partonic structure like a hadron, predicted the occurrence of hard scattering between a gluon from the pomeron emitted by one hadron and a parton from the other hadron, resulting in an event with two high-momentum jets. They recommended looking at this process as away of gaining insight into the structure of the pomeron. The existence of these events was confirmed by UA8 [15].

1.3.2   Diffractive processes at HERA

Deep-inelastic events with a rapidity gap (Fig. 1.8.) in the forward direction have been observed by both ZEUS and H1 (see Fig. 1.9.). These indicate a colourless-singlet exchange between the virtual photon and the proton, which is
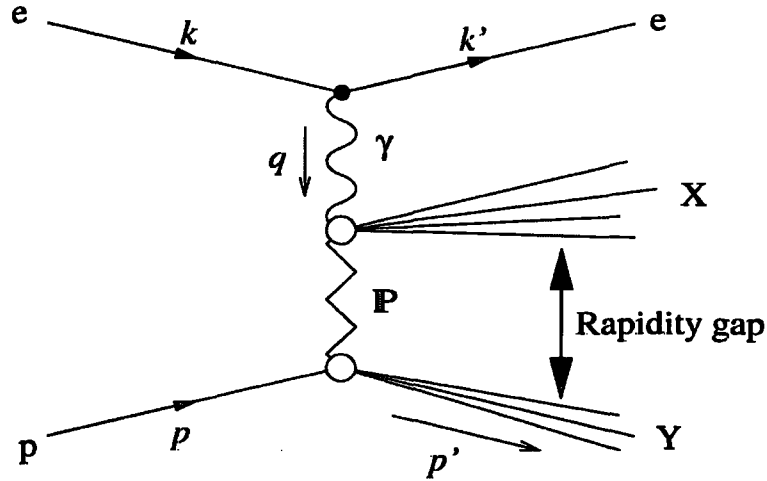
14

Figure 1.8: A schematic diagram of the process leading to formation of a rapidity gap

scattered elastically or dissociates into a low-mass state and is lost in the beam pipe.

The scattered proton, which has very small transverse momentum $p_\perp \approx \sqrt{t}$ could be detected in the years 1999/2000 with the Forward Proton Spectrometer (FPS) indeed, but it has not been used in this analysis because of its low acceptance. Instead, the presence of a rapidity gap extending up to the beam pipe is used as a signature of diffractive exchange. This is quantified using the variable η_{MAX}, defined as the pseudorapidity (for more details, see Sec. 2.2.)

$$\eta = -log\left(tan\frac{\theta}{2}\right) \tag{1.18}$$

of the most forward energy deposit of more than 400 MeV. A small η_{MAX} indicates a large rapidity gap. The number of events with large rapidity gaps is much greater than predicted by a "standard DIS" Monte Carlo generator, which produces large rapidity gaps only as a rare statistical fluctuations in the hadronization process (see Fig. 1.10).

The clear separation of the hadronic final state into two systems X and Y, as labelled in Fig. 1.8, allows three further kinematic quantities to be defined, in addition to those used in standard DIS (Sec. 1.2):
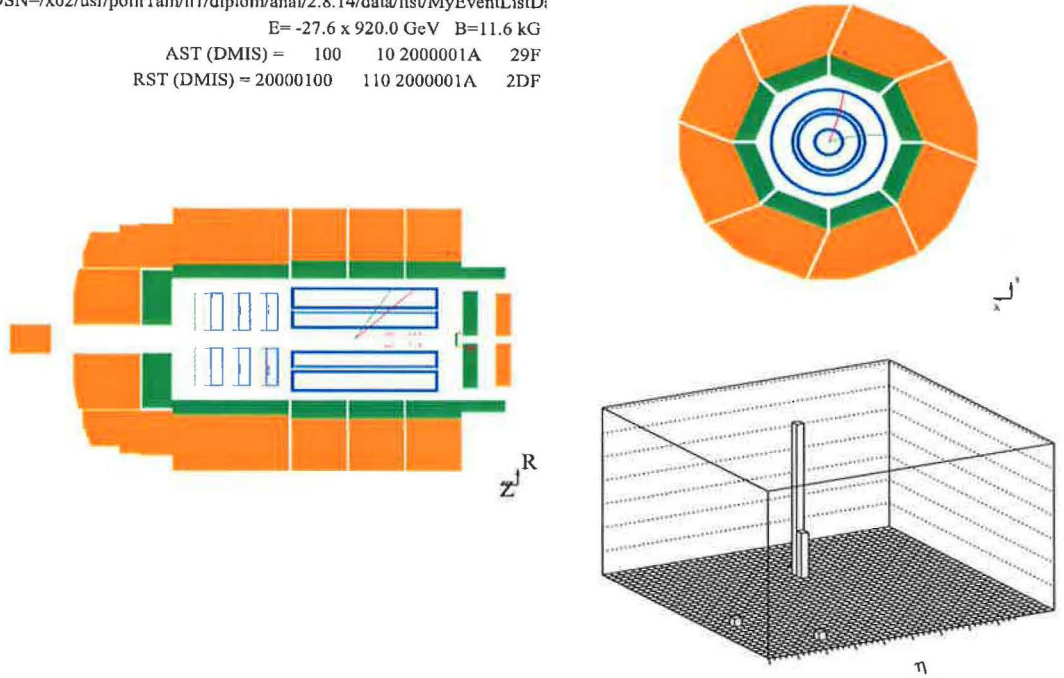
$$t = (p - p')^2 \tag{1.19}$$

15

Figure 1.9: Example of a diffractive event in the H1 detector. This event comes from the analysis described in this thesis.

$$x_{I\!P} = \frac{(p - p') \cdot q}{p \cdot q} \simeq \frac{M_X^2 + Q^2}{W^2 + Q^2} \tag{1.20}$$

$$\beta = \frac{x}{x_{I\!P}} = \frac{Q^2}{M_x^2 + Q^2}. \tag{1.21}$$

The Mandelstam variable t is the squared momentum carried by the colourless exchange object (the pomeron in the Regge picture). The variables β and $x_{I\!P}$ are analogous to x and y. Like the x for the proton, the β is the fraction of the momentum of the pomeron going into the hard subprocess (interacting with the virtual photon). In the limit $t \to 0$, $x_{I\!P}$ is the fraction of the momentum of the proton carried away by the pomeron.

The contribution of diffractive events with an elastically scattered proton can be quantified by defining a diffractive structure function $F_2^{D(4)}$, analogous to the inclusive proton structure function F_2:

$$\frac{d^4\sigma_{ep \to epX}}{dx dQ^2 dx_P dt} = \frac{4\pi\alpha^2}{xQ^4} \left(1 - y + \frac{y^2}{2[R^{D(4)}(x, Q^2, x_{I\!P}, t)]}\right) F^{D(4)}(x, Q^2, x_{I\!P}, t) \tag{1.22}$$
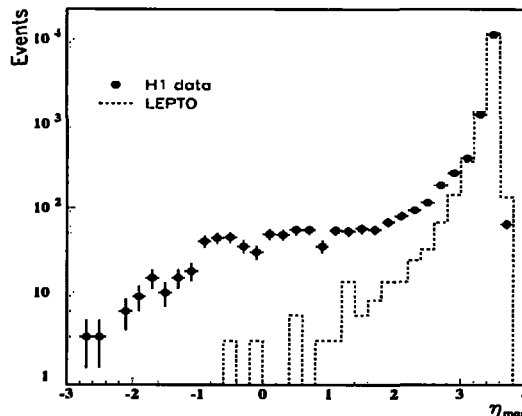
16

Figure 1.10: Distribution of measured η_{MAX} for DIS events, compared with the expectation of a "standard DIS" model (LEPTO)[8].

In this analysis, t cannot be measured since the scattered proton is not detected, so the measured cross section is actually an integral over t up to $|t| \approx 1\ GeV^2$. This limit is determined by the requirement that the proton remnant is not detected.

Some models, such as that of Ingelman and Schlein[14], feature a factorizable diffractive structure function

$$F_2^{D(3)} = F_2^P(\beta, Q^2) \cdot f_{P/p}(x_P) \qquad (1.23)$$

where F_2^P is the structure function of the pomeron and the *flux factor* $f_{P/p}$ describes the pomeron content of the proton. This makes sense in a picture where the pomeron is a hadronic object that is emitted by the proton and then probed by the virtual photon in a hard interaction. Although initial results [16] were consistent with factorisation, a more recent study using higher statistics [17] shows that factorisation in this simple form does not hold. This may simply be because there is a contribution at larger x_P from meson exchange. The results are consistent with the sum of two individually factorizable components - one from a meson trajectory and one from pomeron exchange. However, it may be that even the purely diffractive (pomeron-exchange) component does not factorise, due, for example, to multiple pomeron exchange, or to a failure of the picture of the pomeron as a particle-like object.

17

1.3.3 Models of Hard Diffraction

There are several models describing the jet production in the hard diffraction. The most important for this analysis, the Ingelman-Schlein model and the model from J. Bartels, will be shortly described in this section.

Model of Ingelman-Schlein

The model of Ingelman-Schlein[14] is based on the idea of factorisation. This means that the cross section of a hard diffractive process can be written as a product of non-perturbative (soft) factor describing the emission of a pomeron by the proton and a perturbative factor for describing the hard interaction of a parton from the pomeron with a virtual photon. This process can form one jet in the final state. Two jets can be produced taking into account higher-order QCD processes: the BGF and QCDC (see Sec. 1.2.2).

Model of J. Bartels

J. Bartels used an other approach to model the hard diffraction [20]. The perturbative QCD has been used, the exchange of two gluons represented the required colourless singlet. The main difference is that in this model the pomeron is not treated as a object emitted from the proton but as a gluon-bound state (Fig. 1.11).
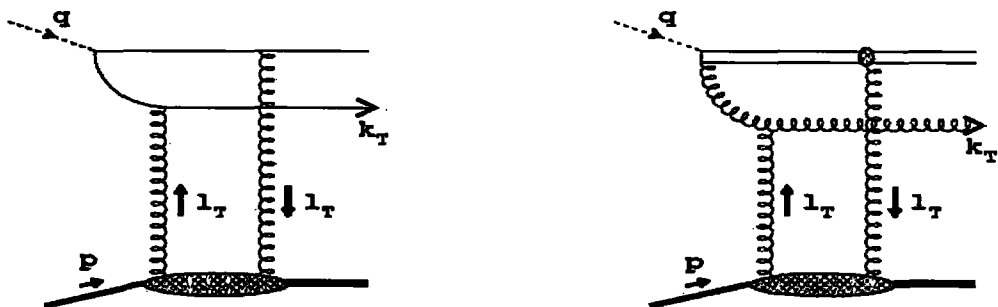

Figure 1.11: Two gluon exchange schemes

High-order QCD contributions to diffractive exchange are expected to be dominated by a *gluon ladder*, illustrated in the Fig. 1.12. This is the diagram described by the BFKL equation [18] and is known as the *BFKL pomeron*. In Regge picture, it corresponds to a fixed singularity [18]:
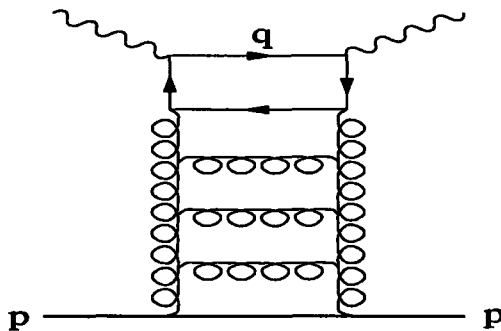
18

Figure 1.12: A gluon ladder, corresponding to a pomeron exchange in the BFKL treatment.

$$\alpha(t) = 1 + \frac{12\alpha_s \ln 2}{3} \qquad (1.24)$$

with $\alpha(0) \approx 1.5$ and called also *hard* pomeron.

1.4 Azimuthal distribution

The quantity which is sensitive to the difference of the models from Sec. 1.3.3 is azimuthal distribution ϕ of the two jets in the $\gamma I\!P$ centre-of-mass system. In this system, the jets are back-to-back and define a so called *jet plane*. The ϕ angle is then defined as the angle between the jet and the lepton plane as on the Fig. 1.13 for the di-pions. Since the ϕ angle is defined in the transverse plane and assuming the pomeron being collinear with the beam proton, one can use not $\gamma I\!P$ but γp centre-of-mass system.

Having the ϕ angle defined in such a way it is obvious that one can restrict himself only to the $0° < \phi < 180°$ range, because of the symmetry - the angle of two planes can be anytime taken as the one with smaller value. This symmetry assumption will finally help to increase statistics and make the wanted effects more visible.

The theoretical predictions of ϕ distribution differs for the two models. While the BGF predicts a clear minimum at $\phi = 90°$, the two gluon exchange model, namely the $q\bar{q}$ configuration, predicts a clear maximum at this value (see Fig. 1.14).

The basic question in this analysis is, whether it is possible to extrapolate the ϕ behaviour from di-jets to di-pions [19]. The aim of this analysis is to study the ϕ distribution of nonresonant di-pions. The main question is whether the
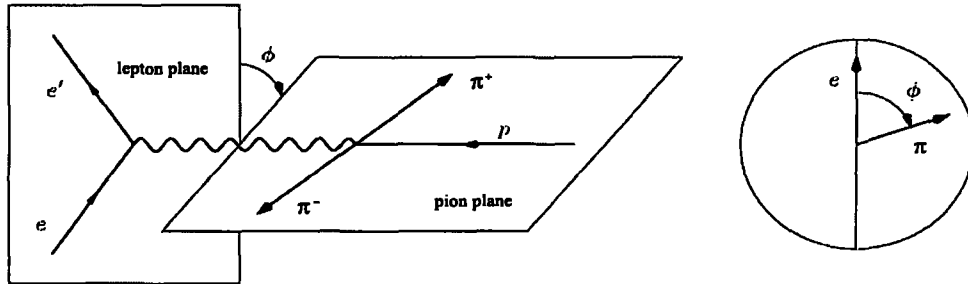
Figure 1.13: Definition of the azimuthal angle ϕ for nonresonant di-pion production.

similarity with di-jets can help to describe the di-pion production either with model of Ingelman-Schlein or of J. Bartels like it was checked for di-jets [23].

The exclusive di-pion production was studied also by the ZEUS collaboration [22] to determine the hadronic component of the photon light-cone wave function.

Figure 1.14: Comparison of the behaviour of the ϕ distribution [21].

20

Chapter 2

HERA and the H1 Detector

2.1 The HERA Accelerator

2.1.1 Introduction
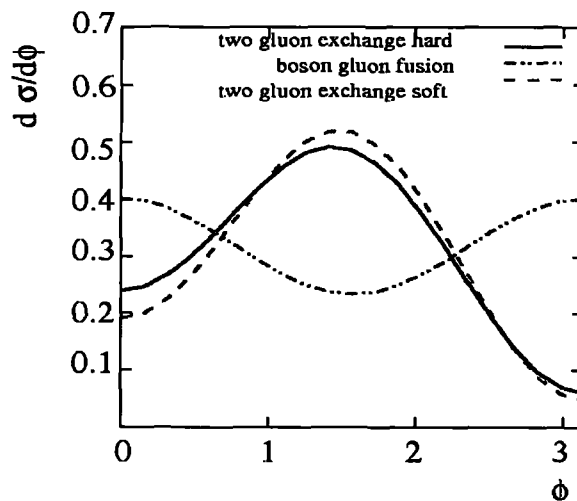
The HERA[1] ring at DESY[2] is a facility for simultaneous acceleration of electrons/positrons and protons. This fact implies that there exist two independent storage rings, one for each particle type. This rings are placed in an underground tunnel of 6.3 km circumference. In the first period of data taking from 1994 to 1997 HERA was operating with 27.5 GeV positrons and 820 GeV protons, since upgrade in 1998 the proton energy increased to 920 GeV. This corresponds to the central-mass-energy of the colliding beams to $E_{CMS} = \sqrt{s} \sim 319~GeV$. With such high energies available, HERA provides usage of electrons as probes for investigating the inner structure of the proton.

2.1.2 Basic Characteristics

The beams consist typically of 180 bunches which collide every 96 ns. The beams are bound by strong magnetic fields generated by the dipole and quadrupole magnets placed along the beam-pipe. Both, the electrons and protons, have their unique field settings. The electrons are bend by conventional dipole magnets with strength of 0.17 T, while for the protons superconducting magnets with field strength up to 4.5 T are used.

One of the important quantities for estimating the quality of the beam is luminosity. The goal of every upgrade is to enlarge the amount of luminosity taken in every running period. Computing of luminosity depends on such beam characteristics as number of bunches, revolution frequency, numbers of particles in

---

[1]Hadron-Elektron-Ring-Anlage
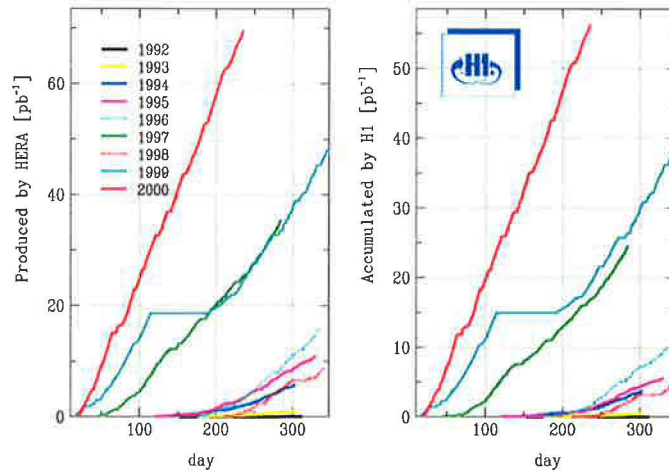[2]Deutsches Elektronen Synchrotron

Figure 2.1: Integrated luminosity produced by HERA (left) and taken by H1 (right) in years 1992 - 2000.

bunch and transverse size of the beam. To estimate, how successful a run period was, the integrated luminosity is introduced. This is luminosity summarised for some time interval. For comparison, the Fig. 2.1 shows the integrated luminosity during the years 1992 to 2000[3].

2.1.3 HERA Experiments

The schematic view of the DESY site is in the Fig. 2.2. There are two beam intersection points at HERA - in the north and in the south hall. There is a big 4π detector at each crossing - the H1 experiment in the Hall North and the ZEUS experiment in the Hall South. These detectors have different properties, but because of their coverage of the interaction point region they are quite universal. Several physical topics are studied with H1 and ZEUS, the main are listed below:

- precision measurements of proton structure functions

- the diffraction phenomena

- heavy flavour production

- structure of the photon

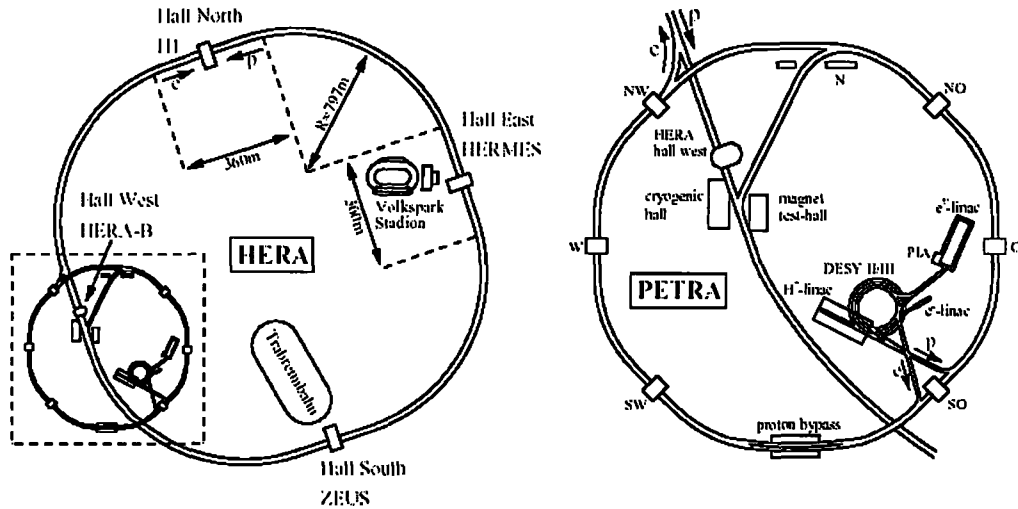[3]Data used in this analysis are from years 99/00

Figure 2.2: The HERA collider (a) and its pre-accelerators (b)

- measurements of α_s

- physics beyond Standard Model

- search for substructures of quarks and leptons

On the other hand, the two remaining experimental sites are using the setting of an experiment with fixed target.

HERMES is located in the Hall East and uses only the electron beam for measuring the spin structure functions of the proton and the neutron. Polarised probes of hydrogen or helium are inserted into the longitudinally polarised beam.

The HERA-B experiment was located in the Hall West and it stopped data taking in 2003. This experiment used the halo of the proton beam to investigate the CP violation in the B-meson physics.

2.2 The H1 Detector

The schematic view of the H1 experiment is in the Fig. 2.3. From the character of the HERA project it is obvious that the detector must be assymetric along the beam pipe. The main task of the experiment is to shatter the incoming proton by the electron, so one expects much more final states in the forward direction

23

HERA Experiment H1
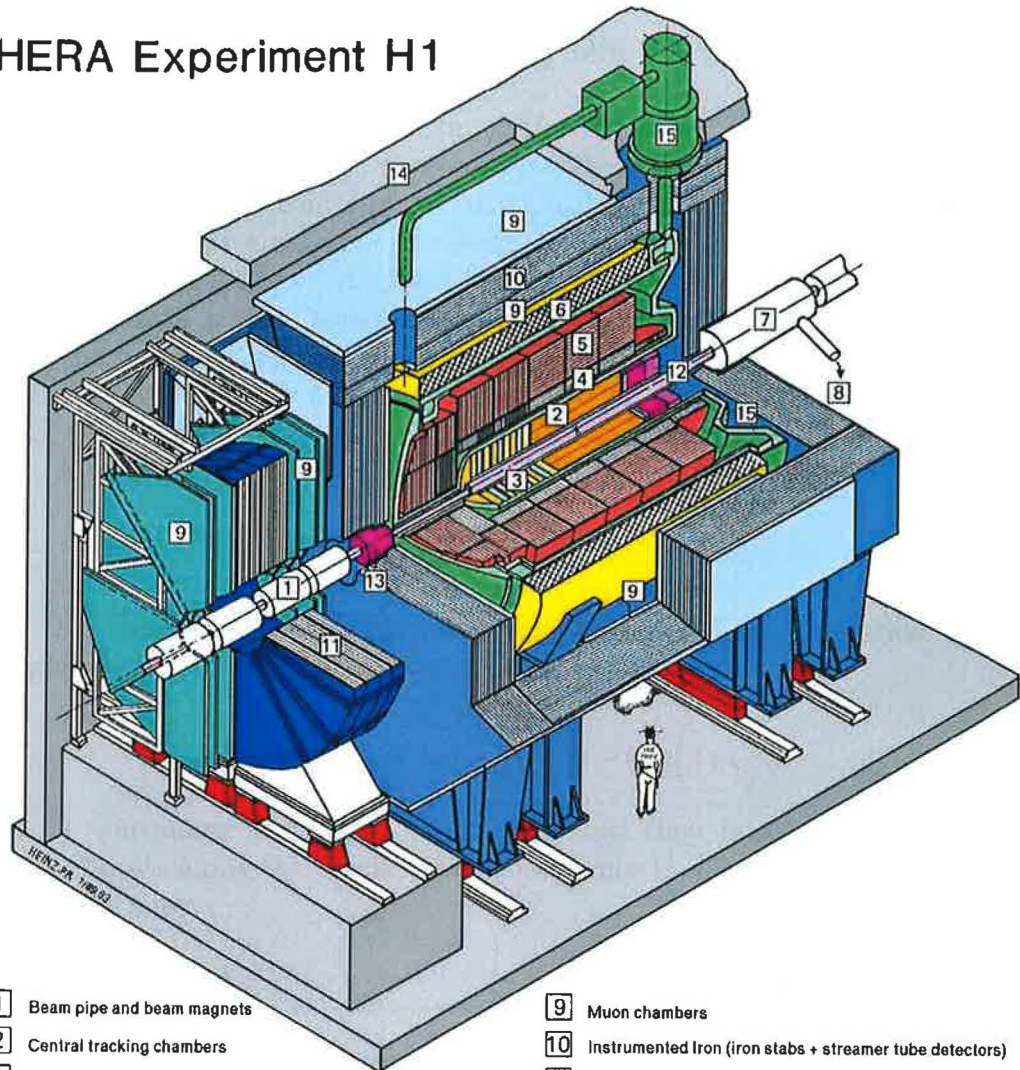
1	Beam pipe and beam magnets	
2	Central tracking chambers	
3	Forward tracking and Transition radiators	
4	Electromagnetic Calorimeter (lead)	} Liquid Argon
5	Hadronic Calorimeter (stainless steel)	
6	Superconducting coil (1.2T)	
7	Compensating magnet	
8	Helium cryogenics	

9	Muon chambers
10	Instrumented Iron (iron stabs + streamer tube detectors)
11	Muon toroid magnet
12	Warm electromagnetic calorimeter
13	Plug calorimeter (Cu, Si)
14	Concrete shielding
15	Liquid Argon cryostat

Figure 2.3: The schematic view of the H1 detector

24

(= along the direction of the outgoing proton). This results in much higher granularity in the forward region.

The detector has size of 12m x 10m x 15m and weight of 2800t. The electrons enter from the left, protons from the right into the interaction region when looking from the centre of the HERA-ring. The coordinate system is defined such that the positive z-axis points along the proton beam direction. The nominal interaction point is at $z = 0$. The x-axis points towards the centre of the HERA ring, the y-axis points upwards. A spherical coordinate system is often used where the polar and azimuthal angles θ and ϕ are defined in the (y,z) and (x,y) planes respectively such that $\theta = 0°$ corresponds to the positive z direction and $\phi = 0°$ points along the x-direction.

A characteristics called *rapidity* is often used. It is defined as follows:

$$y = \frac{1}{2} log\frac{E + p_z}{E - p_z} = \frac{1}{2} log\frac{(E + p_z)^2}{m^2 + p_t^2} \tag{2.1}$$

For massless case, the *pseudorapidity* η is used. The derivation from y is straightforward:

$$\eta = y_{|m=0} = log\frac{E + p_z}{p_t} = -log\left(tan\frac{\theta}{2}\right) \tag{2.2}$$

A convenient feature of η and y is that they transform linearly under Lorentz boosts along the z-axis. The consequence is that Δy or $\Delta \eta$ are invariant under such boosts.

2.2.1 Tracking

The H1 tracking system covers almost whole angular range $5° < \theta < 178°$ and the whole azimuthal range. It is subdivided into several parts:

Silicon Trackers

Very close to the interaction point, the central and backward silicon trackers CST and BST[4] are installed.

Central Tracking System

The next layer is composed by two large concentric drift chambers (CJC1 and CJC2)[5] with a length of 2.2m. The drift cells are inclined by about 30° with respect to the radial direction. The chambers are made of cells with sense wires,

---

[4] Central and Backward Silicon Tracker
[5] Central Jet Chamber

25

strung parallel to the z-axis. The resolution in the radial direction is approximately 100 times better than in the z-direction. These devices are completed by some additional MWPCs[6].

Forward Tracking

The forward tracking system consists of three identical planar and radial drift chambers, a proportional chamber and a transition radiator.

Backward Tracking

Tracking information in the backward region is provided by the BDC[7], which was installed in H1 as part of a major detector upgrade in 1995. Its main purpose is to measure the direction of the scattered electron.

2.2.2 Calorimetry

The H1 detector consists of four calorimeters: The Liquid Argon Calorimeter (LAr), the backward **Spaghetti Calorimeter** (SpaCal), the so-called **Tail Catcher** (TC) and the PLUG calorimeter, which is placed around the forward beam pipe.
The TC and PLUG are not used in this analysis.

Liquid Argon

The LAr sampling calorimeter has two parts - the inner electromagnetic and outer hadronic. This setting is because of the evolution of the particle shower by passing through matter. The main advantages of the LAr are good stability, homogenity of the response, ease of calibration and fine granularity which can be achieved. It is segmented along the z-axis into eight wheels. Each wheel is segmented into eight octants, the total number of readout channels is about 45 000.

The electromagnetic part consists of 2.4mm thick lead absorber plates with 2.35mm liquid Argon as active material, leading to a thickness of 20 to 30 radiation lengths. The energy resolution for electrons has been determined as $\sigma_{em}(E)/E \simeq 11\%/\sqrt{E[GeV]} \oplus 0.01$. The hadronic section consists of 19mm stainless steel absorber plates with a double gap of 2.4mm LAr, the energy resolution is $\sigma_{had}(E)/E \simeq 50\%/\sqrt{E[GeV]} \oplus 0.02$. The LAr calorimeter is non-compensating, i.e. the response to hadrons is about 30% smaller than that to electrons of the same energy. This is corrected by the off-line reweighting.

---

[6]**Multi Wire Proportional Chamber**
[7]**Backward Drift Chamber**

26

Spaghetti Calorimeter

The second calorimeter very important for this analysis is the SpaCal calorimeter. It provides information about the energy deposited in the backward region of the H1 detector and is therefore very important by determinating the scattered electron energy. The calorimeter has two parts - the electromagnetic and the hadronic. The cells in the e.m. section have very small size, so the electron-pion separation and position resolution is very good. The energetic resolutions are $\sigma_{em}(E)/E \simeq (7.1 \pm 0.2)\%/\sqrt{E[GeV]} \oplus (1.0 \pm 0.1)\%$ and $\sigma_{had}(E)/E \simeq 30\%/\sqrt{E[GeV]}$.

2.2.3 Forward Detectors

In case of diffractive processes, such as searched for in this analysis, the forward detectors are very important. These detectors can provide a valuable information about the particles going in the very forward direction, even if they are not capable of detecting the scattered proton itself.

The Forward Muon Detector (FMD) is situated beyond the return yoke for the magnetic field. Its design purpose is to trigger on and to measure muons in the forward region of H1. It consists of six double layers of drift chambers, four with wires strung tangentially around the beam pipe to measure θ and two with wires strung radially to measure ϕ. Because of secondary scattering with the beam pipe, the FMD has an indirect sensitivity to particle production at pseudorapidity values larger than its direct coverage of $\eta < 3.7$. This is employed for the selection of diffractive events.

The Proton Remnant Tagger (PRT) is located at $z = +24m$ in the forward direction inside the HERA tunnel. It consists of seven scintillators arranged around and between the proton and electron beam pipes. Signals are only considered if they are within the time window expected from an ep interaction. The PRT is sensitive to particles produced in the pseudorapidity range $6 < \eta < 7.5$.

2.2.4 Other Installations

Around the LAr calorimeter there is the superconducting coil of field strength 1.15T which provides a homogeneous field for the central region of the H1 detector. The outer region of H1 consists of Muon detector, which is made of iron and plastic tubes with signal wires. This part of the experiment is not used in this analysis.

2.2.5 Trigger System

The bunch crossing rate inside the H1 detector is 10.4 MHz whereas the physics rate is only about 10 Hz. Since it is technically impossible to readout the whole detector information for each bunch crossing a three level trigger system was designed to reduce subsequently the rate of triggered events such that the readout rate is reasonable small. Only the first and the fourth levels are used in this analysis.

The first level system (L1) is phase-locked to the HERA accelerator clock of 10.4 MHz. The system provides a trigger decision for each bunch crossing after 2.3 μsec without causing a dead time and works on hardware level. A subset of the subdetector system is used by most systems to generate fast informations concerning the general properties of the event. This is encoded in Boolean decisions (Trigger Elements). There are two levels of L1 subtrigger system: *raw* and *actual*.

Raw means that all incoming signals are taken with no prescales. The prescales are multipliers set to each subtrigger element separately. If the prescale is set to N for some element, than this element does not work $(N - 1)$ times and for the last time it multiplies the event with N. The *actual* level on the other hand takes into account the subtrigger prescales and serves to reduce the number of accepted events mainly.

The second level consists of two subsystems: a topological trigger and a trigger based on neural networks. Both systems use the combination of signals from the different detector subsystem. The decision time for this trigger level is 20 μs.

The level three does not exist.

The level four system is not phase-locked to HERA and triggers the events off-line. Therefore its reaction time can be longer, ca. 100 ms. It works only on the software level with the Power PC farms. It filters out obvious background and performs physical event classification.

Chapter 3

The Event Selection

The data used in this analysis are from the years 1999 and 2000. At this time, the protons collided with positrons. By that time, HERA operated at energies 27.5 GeV for positrons and 920 GeV for protons.

The analysis is done in the object-oriented environment. It is called H1OO[1] and is based on the programming languages C and C++. The physics analysis has been done with the analysis tool ROOT, which is also object-oriented. This techniques follow the trend of upgrading the analysis procedure in the whole H1 experiment.

This chapter describes the first level cuts, the subtrigger s61 definition and efficiency, the scattered electron reconstruction, the pion finder and the diffraction and nonresonant cuts.

3.1   The First Level Cuts

Run Quality

The event selection is based on good run selection. The good run is defined as the collection of a sequence of events over a time period with relatively stable beam, detector and trigger conditions. The Run Quality has three levels: good, medium or poor. The cut used in this analysis was

$$RunQuality > 2$$

which means only the good quality.

---

[1] H1 Object Oriented Environment

Kinematical cuts

The DIS kinematic range of the measurement is confined to a region in which the geometric acceptance and reconstruction efficiency are high. The defined kinematic range in terms of Q^2 and y, for all measurements in this thesis, is:

$$4\ GeV^2 < Q^2 < 100\ GeV^2$$
$$0.05 < y < 0.7$$

The low Q^2 range is determined by the geometrical acceptance of the scattered electron in the SpaCal. In the events with $Q^2 > 100\ GeV^2$, the electron is scattered into the liquid argon calorimeter. The triggers used in this analysis contain conditions for the SpaCal calorimeter and will thus reject all events with electron in LAr.

The lower limit for the y restriction rejects the beam-gas background and the upper limit is a result of the cut on the scattered electron energy.

The z-Vertex Position

The design of the beam bunches makes sure that the interaction point in the H1 detector is well defined. The approximative Gaussian distribution of the proton bunches in the longitudinal direction gives a distribution of the collision points around the nominal interaction point. In contrast, events coming from the beam halo and the interactions with the walls are equally distributed along the z-axis. To avoid such interactions that are not coming from the ep collision, the cut

$$|Z_{Vtx}| < 35\ cm$$

is used.

Rejection of Photoproduction Events

In the HERA frame of reference for DIS events the following relation can be established between the energies and the longitudinal momenta of the incoming beams:

$$E - p_z = (E_e + E_p) - (p_{z,e} + p_{z,p}) = 2E_e = 55\ GeV \qquad (3.1)$$

Due to energy and momentum conservation in the diffraction this quantity can be computed via final state particles - the scattered electron and the particles in the M_X system. The particles escaping through the beam-pipe (like the scattered proton) don't contribute to this quantity at all. This leads to an other definition of $E - p_z$:

$$E - p_z = (E'_e + \sum_{hads} E) - (p'_{z,e} + \sum_{hads} p_z) \simeq 55\ GeV \qquad (3.2)$$
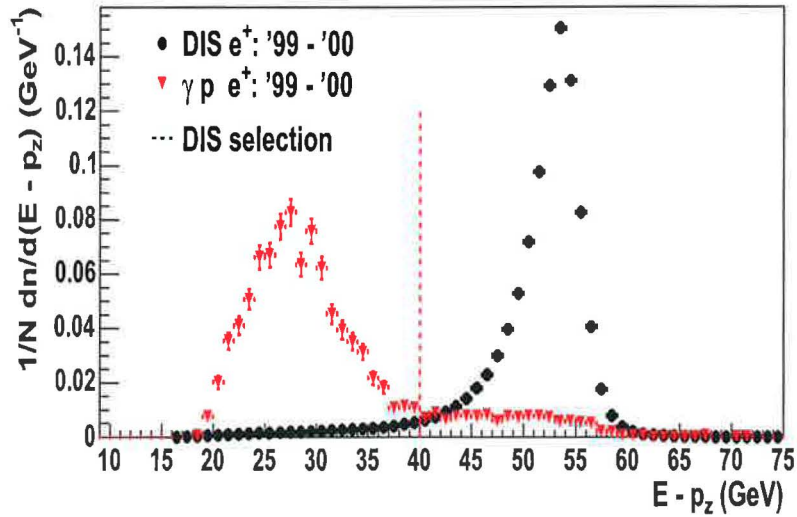
30

Figure 3.1: The illustrative comparison of $E - p_z$ for DIS and photoproduction. The dashed line is the cut which is used in this analysis.

From the Fig.3.1., which shows the $E - p_z$ distributions for DIS and photoproduction events, it is clear to see that the cut $E - p_z > 40\ GeV$ will reduce the background from photoproduction significantly.

3.2 The Subtrigger s61

3.2.1 Definition

The subtrigger is a set of several trigger elements combined in one condition.
The subtrigger s61 has been chosen because it is the trigger element which selects DIS events. For further information see [25]. The definition of the subtriggers changes with the time, the definition of s61 for the years 1999/2000 is following[2]:

$(DCRPh\_THig\&\&zVtx\_sig\&\&(SPCLe\_IET > 2||SPCLe\_IET\_Cen\_3))$
$\&\&(!SPCLh\_AToF\_E\_1\&\&)!SPCLh\_ToF\_E\_2\&\&!VETO\_inner\_BG\&\&$
$VETO\_Outer\_BG\&\&VLQToF\_BG)\&\&$
$(!(DCRPh\_NL\_many\&\&DCRPh\_NH\_many\&\&DCRPh\_PL\_many$
x $\&\&DCRPh\_PH\_many))\&\&((FToF\_IA||FIT\_IA)||(FToF\_BG||FIT\_BG))$

---

[2]The signs "&&","||" and "!"are logical operators in C++

31

The s61 can be split in two main parts. The first part selects the events with good reconstructed momentum tracks (trigger element DCRPh), good z-vertex position (trigger element zVtx_sig) and a deposited energy in electromagnetic part of SpaCal above a certain energy threshold, selected with SPCLe_IET. The second part contains veto conditions reducing the number of background events which might fake the diffractive nonresonant di-pion DIS events.

3.2.2 The Trigger Element Efficiency

Taking into account the subtrigger efficiency is important mainly when the cross section should be determined, in our case the only demand is that the efficiency dependence on various observables studied in this analysis has to be flat. To get it one has to choose an independent subtrigger element as a monitoring trigger and then make two event samples. There is no subtrigger element wholly independent of the s61, for the purposes of this analysis, the s0 was used. For 1999/2000, it is defined as:

$$(SPCLe\_IET > 2)$$
$$\&\&(!VETO\_inner\_BG\&\&VETO\_Outer\_BG\&\&VLQToF\_BG)$$
$$\&\&(((FToF\_IA||FIT\_IA)||(FToF\_BG||FIT\_BG))$$
$$\&\&(PToF\_IA||!PToF\_IA))$$

Compared with the s61, the s0 uses only the SpaCal energy trigger element and some veto conditions.

Efficiency and Subtrigger Level Definition

The subtriggers were not simulated in Monte Carlo, therefore the trigger efficiency will be determined only from the data.

The subtrigger levels were described in Sec. 2.2.5.

Having both subtriggers defined one can compute the efficiency with following formula:

$$Effic = \frac{Signal + s0_{l1act} + S0_{l4v} + S61_{l1raw}}{Signal + S0_{l1act} + S0_{l4v}} \tag{3.3}$$

The term "Signal" means that the efficiencies are computed for some basic variables after the application of all other selection cuts.

In Fig. 3.2. the trigger efficiency dependence on electron energy E_{el} and his azimuthal angle ϕ_{el} and polar and azimuthal angels of both pion candidates are shown. The dependence of efficiency on these variables is computed as a ratio of events with subtrigger combinations fired as in the nominator and denominator in the equation (3.3). The efficiencies of electron and pion candidate angles

are about 60%-70% and can be approximated by a constant. The efficiency of scattered electron energy increases from 25% to 80%. The reweighting has been done by a bin-by-bin method. The inverse value of each bin content from the Fig. 3.2. a) has been taken as a weight and every time the relevant event has been reweighted.
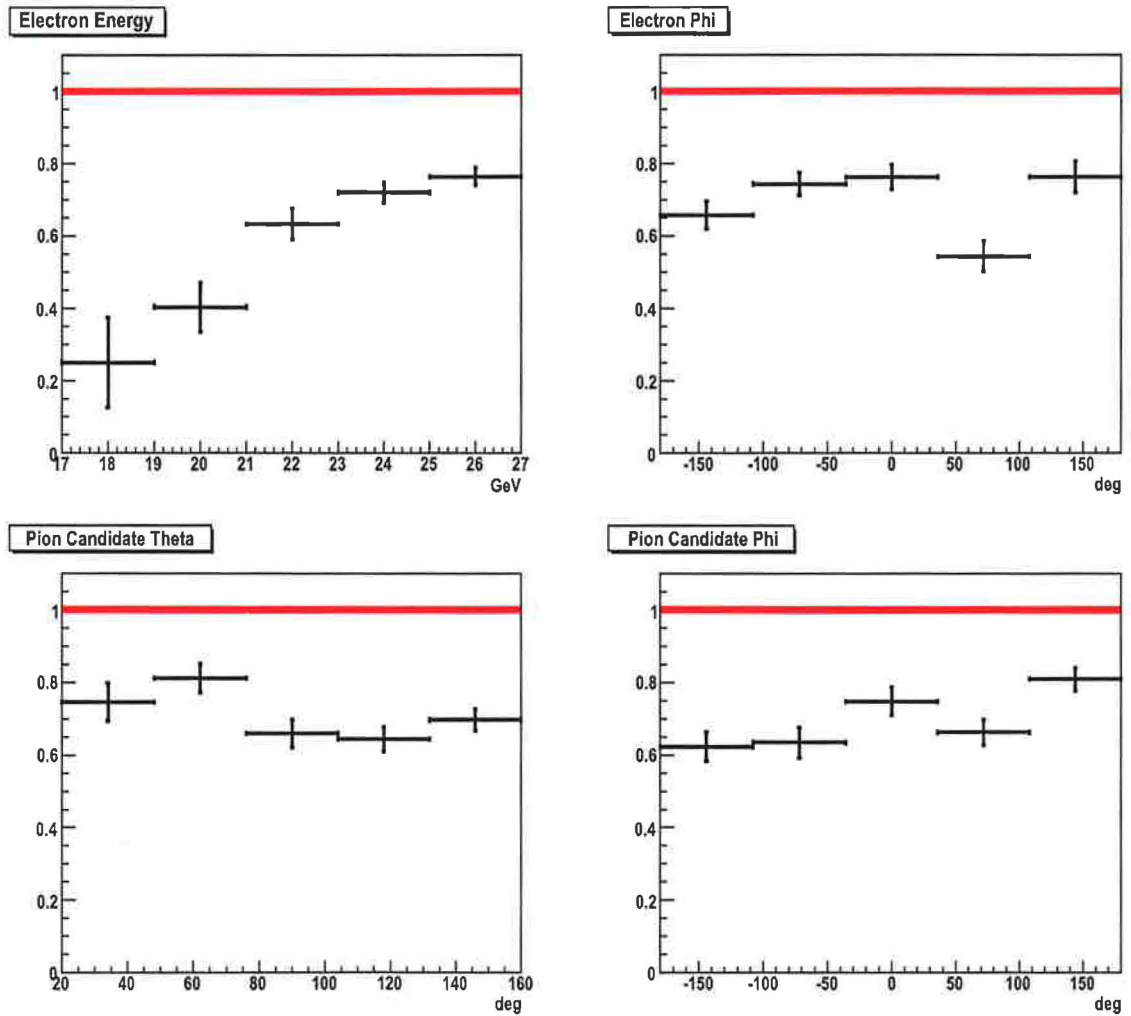

Figure 3.2: The S61 efficiency dependence on electron energy E_{el} and azimuthal angle ϕ_{el} and pion candidate angels θ_{π} and ϕ_{π}

33

3.3 Scattered Electron Selection

This section will focus on the scattered electron measurement. It is very important to have a good agreement of electron variables in data and Monte Carlo as well as a good correlation between reconstructed and generated MC levels. The good precision is required for boosting into the γp centre-of-mass system, the photon kinematics is estimated from the scattered electron.

The selection of the electron is granted by a set of various cuts applied on the particles, which interact mostly in electromagnetic part of SpaCal and are therefore tagged as "electromagnetic particles".

At first, a list with unfunctional regions of SpaCal and a corresponding list of runs was created. These lists were integrated to the selection code and every time the scattered electron hit any of these SpaCal areas, the event has been rejected.

The events with only one particle in electromagnetic section of calorimeters has been selected. This one particle has to be tagged as "Scattered Electron". This tagging is done automatically in the H1OO. For these events, following cuts on the scattered electron have been applied:

- The scattered electron energy $> 17~GeV$

- The energy in Veto layer in Spacal $< 1~GeV$

- The hadronic part of calorimeter shower $< 0.5~GeV$

- The hadronic fraction from the energy of the scattered electron $< 0.03~GeV$

- The $z-$ position of the cluster in SpaCal $> -180~cm$

- The SpaCal cluster radius $< 4~cm$

- The radial cluster position in SpaCal $> 9.1~cm$

- The distance between SpaCal and BDC extrapolation $< 1.5~cm$

The fig.3.3. shows the $x - y$ distribution of the scattered electron in SpaCal for the data which passed through these cuts.

3.4 The Pion Finder

We are interested in the exclusive nonresonant di-pion production, therefore we will reject all events with any neutral energy deposition in calorimeters above a noise level.
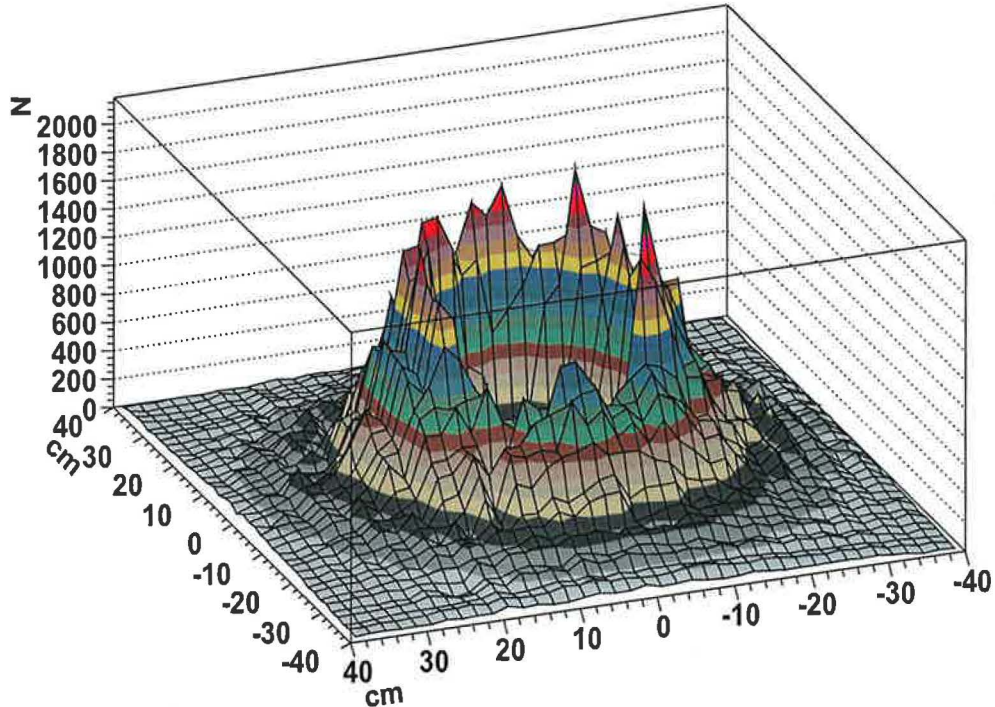
34

Figure 3.3: The distribution of the scattered electron energy clusters in SpaCal in the $x - y$ plane for data selected with the cuts above.

Within the H1OO environment there exist a procedure called Light Vector Meson Finder [24]. This class has been modified for purposes of this analysis and used for the pion candidates selection.

Track Selection

There exist several classes in the H1OO that gather track candidates from all the possible tracking systems (See Sec. 2.2.1.). The most suitable method to find the tracks of interest is the H1PartSelTrack class. This class has several labels that help distinguish the origin of the track.

This class has been checked and all track candidates has been stored into an array. The track of the scattered electron has been removed. This case was rather rare, because the scattered electron in this Q^2 region is mostly detected in the SpaCal and avoids hitting any tracker.

The events with only two tracks with opposite charge originating from

35

the primary vertex have been selected. Both tracks were required to have $p_t > 150\ MeV$ in order to ensure a good momentum reconstruction. Both tracks have to be within the θ_π range of $20° < \theta_\pi < 160°$.

The Neutral Particles Background

The class for all possible particles is called the H1PartCand class and it stores pointers to all possible existing candidates. An array with neutral candidates has been created. To recognise a neutral candidate one had to look if there was no pointer to any track associated, the scattered electron has been excluded.

In a loop through this array we rejected the events where the neutral energy is larger than $400\ MeV$ in LAr and $100\ MeV$ in SpaCal. It corresponds to the level of the electronic noise in both calorimeters. This way, the amount of events with neutral energy has been decreased significantly.

3.5 The Diffractive Event Selection

The η_{MAX} cut widely applied to select diffractive events was used in a following way: the two tracks has been sorted in the increasing θ_π order and ($\theta = 0°$ is in the direction of the outgoing proton). The cut on such "forward" track has been applied:

$$\eta_{forward} < 3.2$$

The selection of diffractive events is based on the absence of activity in Forward Muon Detector (FMU) and Proton Remnant Tagger (PRT) (see Sec. 2.2.3.) Following cuts have been done:

$$NFMU[0] + NFMU[1] < 2$$
$$NFMU[2] < 2$$
$$NPRT[i] = 0,$$

which means that in the first two layers as well as in the third layer of the Forward Muon Detector there was only one hit allowed. The first five ($i = 0..4$) layers of PRT should be without any signal.

The cut

$$x_{I\!P} < 0.04$$

is used to reduce the events where the reggeon exchange dominates.

3.6 Invariant Mass Distribution

The Fig. 3.4. shows the invariant mass spectrum of two pion candidates for data events selected by cuts mentioned above. The main contribution to the invariant mass spectrum comes from the ρ resonance with mass $M_\rho = 775.8 \pm 0.5\ MeV$ [29]. The cut

$$1.1\ GeV < M_{\pi\pi} < 3.0\ GeV$$

significantly reduces the resonant background from ρ and also J/Ψ production.

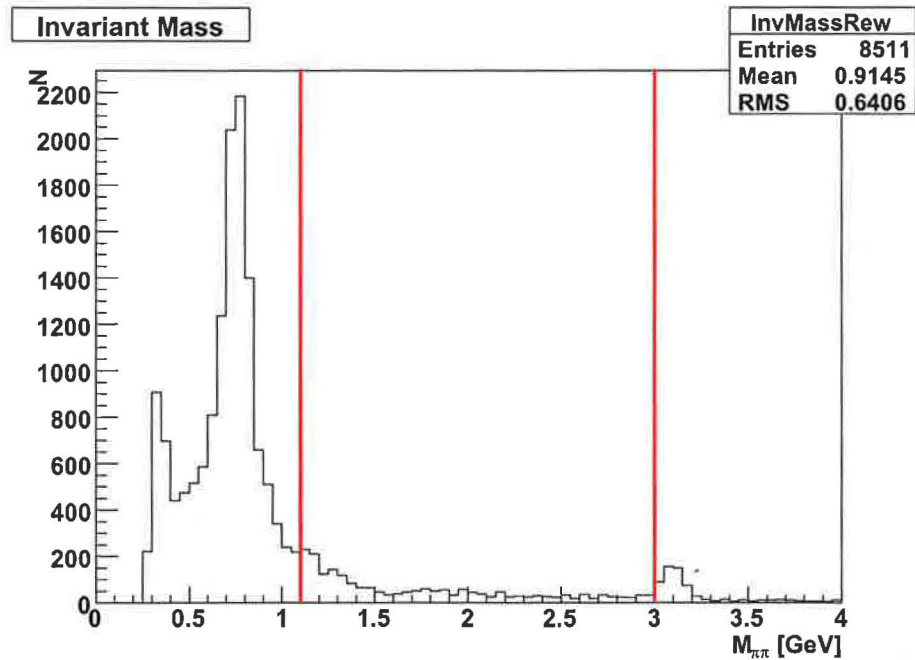After all these cuts, 996 events remained from the original sample of data from the time period 1999/2000.

Figure 3.4: The invariant mass of the two pion candidates (the $M_{\pi\pi}$ system). The red lines show the applied cut.

37

Chapter 4

Monte Carlo

This chapter describes the reconstruction methods of Q^2 and y variables and the choice of the most precise one. The next section presents the comparison of electron and pion candidate characteristics on detector and hadron level. Finally it describes the attempt to find additional cuts which could help separate the nonresonant di-pion events from all others.

Two sets of Monte Carlo generated events have been used.

4.1   Pomeron Exchange Monte Carlo Files

The Monte Carlo files based on the Pomeron Exchange Model (PEM) has been generated with RAPGAP 2.08 [27]. These files were used for analysis of multiplicities studies in diffractive DIS [28].

Three files have been generated - the first one with the u, d and s quarks contains about 5 million of events, the second one with the charm production 500,000 and the third one generated via meson exchanges 5 million of events. The request for exclusive $\pi^+\pi^-$ excludes theoretically the presence of c-quarks. This fact was confirmed, no event from the c-quark file passed through the selection. The result of the meson file selection was about one hundred events. From the first file, finally 71 000 events before the invariant mass cut passed through the selection. After this cut 24358 events remained and therefore finally only this file was used for the analysis.

4.2   Two Gluon Exchange Monte Carlo Files

The two files simulating events according to the Two Gluon Exchange model (TGE) have been generated with the RAPGAP 2.08, too. The first file was generating the $q\bar{q}$ configuration and the second the $q\bar{q}g$ one. Both of them contained

1 million events[23]. After the selection cuts we obtained 3346 events for file with $q\bar{q}$ configuration and no event for the $q\bar{q}g$ configuration. Only the $q\bar{q}$ file was finally used for comparison with the data.

4.3 Kinematic Reconstruction

There are several methods for determination of the Q^2 and y variables. The three most used are described and compared in this section and the best method is chosen. The first method uses the electron kinematics, the second the hadronic final state and the third combines both of them.

The Electron Method

In the case of electron method, only the four vector of the scattered electron is used:

$$Q^2 = -(k - k')^2 = 2EE'(1 + \cos\theta) \tag{4.1}$$

$$y \equiv \frac{p \cdot q}{p \cdot q} = 1 - \frac{E_p E' - E_p E' \cos\theta}{2EE_p} = 1 - \frac{E'}{2E}(1 - \cos\theta) \tag{4.2}$$

where E is the incoming electron energy, E' the scattered electron energy, θ_{el} the scattering angle of the electron and E_p is the incoming proton energy. The four-momenta are defined in Sec. 1.2.

Using Q^2 and y one can get x:

$$x = \frac{Q^2}{4EE_p y} \tag{4.3}$$

The Q^2 can be also determined by follows:

$$Q^2 = \frac{E'^2 \sin^2\theta}{1 - y} = \frac{p_{Te}^2}{1 - y} \tag{4.4}$$

where p_{Te} is the transverse momentum of the scattered electron.

The Hadronic Method

The other possibility of obtaining the Q^2, y and x variables is if one measures all the outgoing hadrons:

$$y = \frac{p \cdot (p_h - p)}{p \cdot k} = \frac{p \cdot p_h}{2EE_p} = \frac{E_h - p_{zh}}{2E} \tag{4.5}$$

39

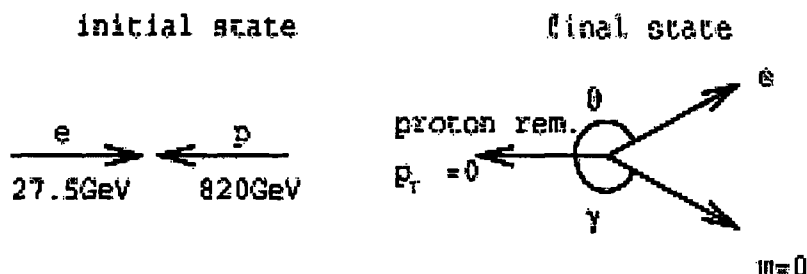initial state   final state

Figure 4.1: The two angles used in the double angle method

where p_h is the four-momentum of all outgoing hadrons, E_h is their energy and p_{zh} their p_z.

It is obvious that the escaping hadrons have a small p_T, their contribution to $E_h - p_{zh}$ is negligible and thus one gets a good estimate of y using this formula. The other two variables can be now calculated in the following way:

$$Q^2 = \frac{p_{xh}^2 + p_{yh}^2}{1 - y} \tag{4.6}$$

$$x = \frac{Q^2}{4EE_p y} \tag{4.7}$$

The Double Angle Method

When using a method based on a mixture of the electron and hadron variables, one can choose different combinations. The one described here is called the double angle (DA) method and uses measurements of two angles. The first angle is the scattering angle θ of the outgoing electron (see Fig.4.1.) and the second angle is that of an object which has a simple meaning in the naive parton model: assuming that the struck parton is massless, it would scatter by an angle γ. In this interpretation, the p_T of the proton remnant is zero. Note that these assumptions are necessary only for the physical interpretation of the angle γ. The calculation is however exact.

Now the four vector of the scattered electron k' and that of the mathematical massless object Γ is defined as follows:

$$k' = (\ E',\quad E'\sin\theta,\quad 0,\quad E'\cos\theta\ ) \tag{4.8}$$

$$\Gamma = (\ \Gamma,\quad \Gamma\sin\theta,\quad 0,\quad \Gamma\cos\theta\ ) \tag{4.9}$$

Now the variables y and Q^2 computed with the hadronic and the electron method can be expressed in terms of k' and Γ. The final relations are less sensitive to a
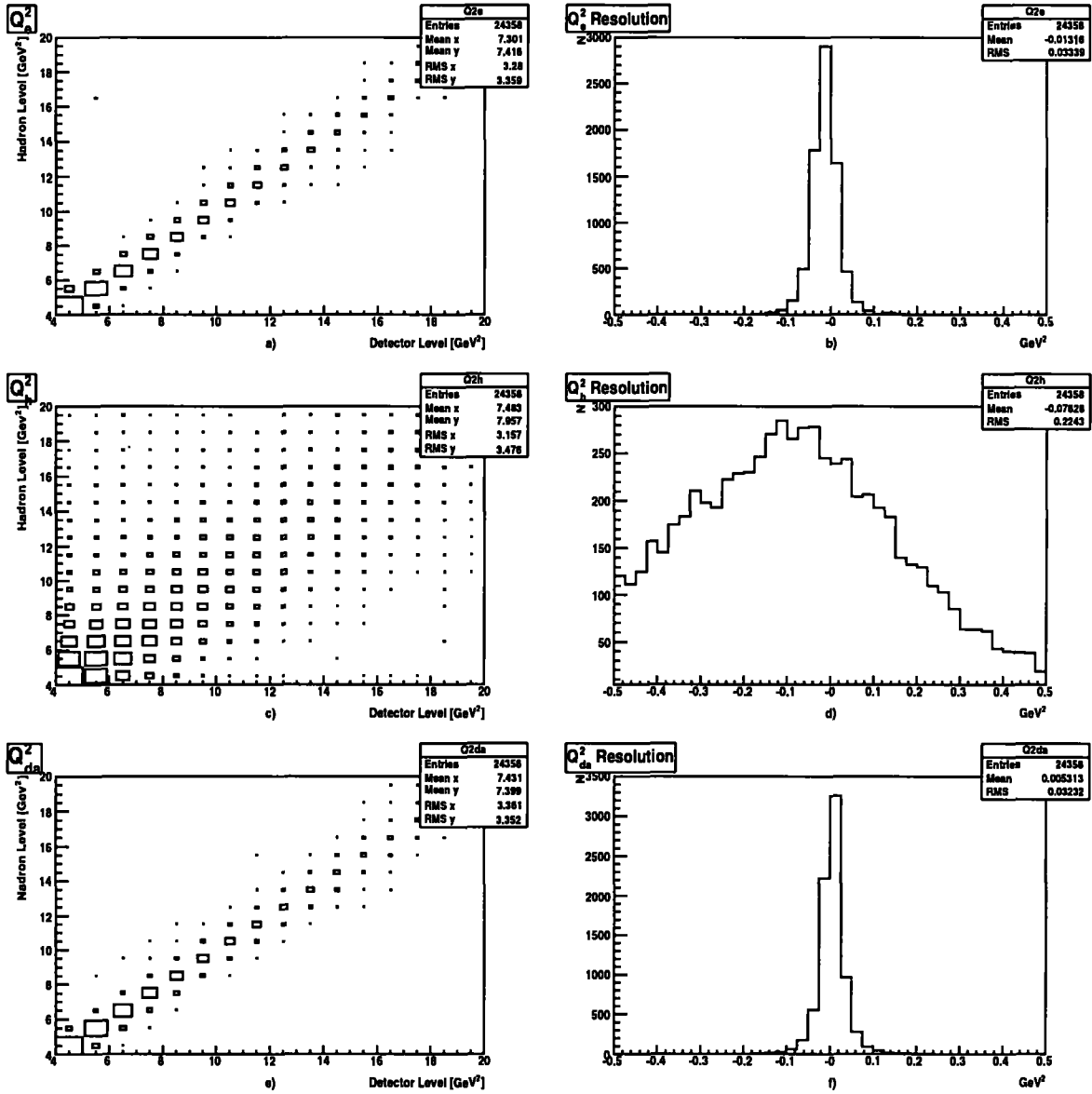
Figure 4.2: The comparison of Q^2 reconstruction methods: a) and b) the electron method, c) and d) the hadron method and e) and f) the double angle method.
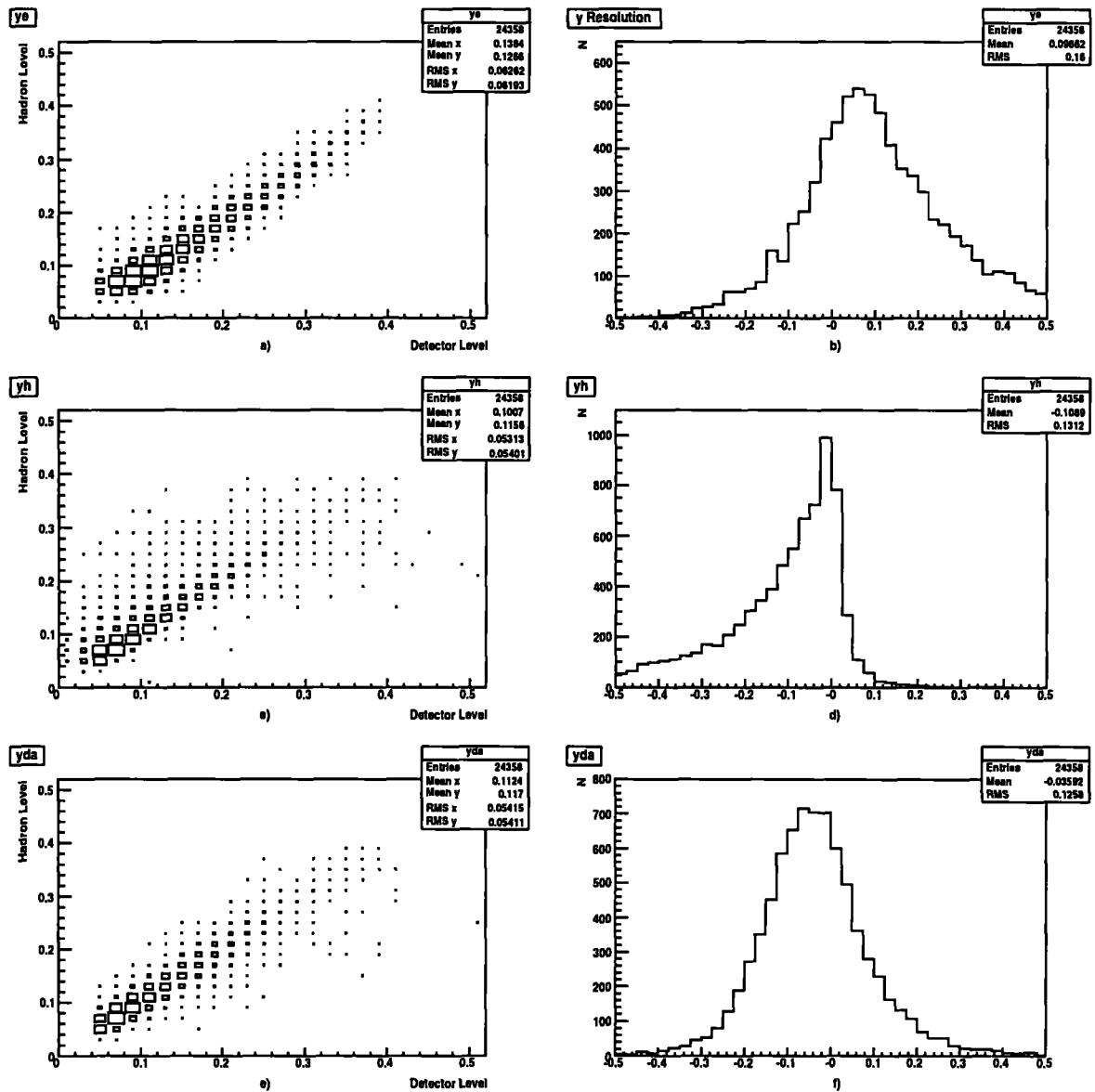
Figure 4.3: The comparison of y reconstruction methods: a) and b) the electron method, c) and d) the hadron method and e) and f) the double angle method.

42

scale uncertainty in the energy measurement of the final state particles since the angle γ is obtained by the ratios of energies. The Q^2 and x can be obtained as follows:

$$Q^2 = 4E^2 \left[\frac{\sin\gamma(1+\cos\theta)}{\sin\gamma + \sin\theta - \sin(\theta + \gamma)} \right] \qquad (4.10)$$

$$x = \left(\frac{E}{E_p} \right) \left[\frac{\sin\gamma + \sin\theta + \sin(\theta + \gamma)}{\sin\gamma + \sin\theta - \sin(\theta + \gamma)} \right] \qquad (4.11)$$

The Comparison of Methods

On Fig. 4.2. and 4.3. the correlation plots for events generated by MC RAPGAP 2.08 (resolved pomeron file) at generated and reconstructed level for Q^2 and y determined by all three methods are shown. In the right column, the resolution defined as $\Delta x/x$ where Δx = reconstructed - generated value and x is the generated value. It is evident that the best method should have the maximum closest to zero and it should have the smallest width of the resolution distribution.

From the Fig. 4.2 it is clear that the Q^2 electron and double angle method give a good resolution. The double angle method is slightly preferred and will be therefore used. According to the Fig. 4.3, the best method for describing the y variable is the double angle method again.

4.4 The Quality of Electron Reconstruction

This section analyses the quality of the scattered electron reconstruction. Monte Carlo sample of events generated with PEM was obtained after all applied cuts described above. The Fig. 4.4 shows the electron energy E_{el}, θ_{el} and ϕ_{el} correlation at detector and hadron level in the left column and the resolution in the right column.

The resolution is determined as $\Delta x/x$ in the case of the electron energy and Δx = reconstructed - generated value for the θ_{el} and ϕ_{el} distributions. The resolution of θ_{el} and ϕ_{el} distributions is rather good, the energy resolution is not perfect, mainly because of the initial and final state radiation. The electron can radiate a photon, before as well as after the emission of the exchange boson. In this case the scattered electron is composed of the scattered electron and of the final state radiated gamma. This gamma can be lost in the beam-pipe or it builds one cluster in SpaCal together with the scattered electron. This fact makes the correlation worse.
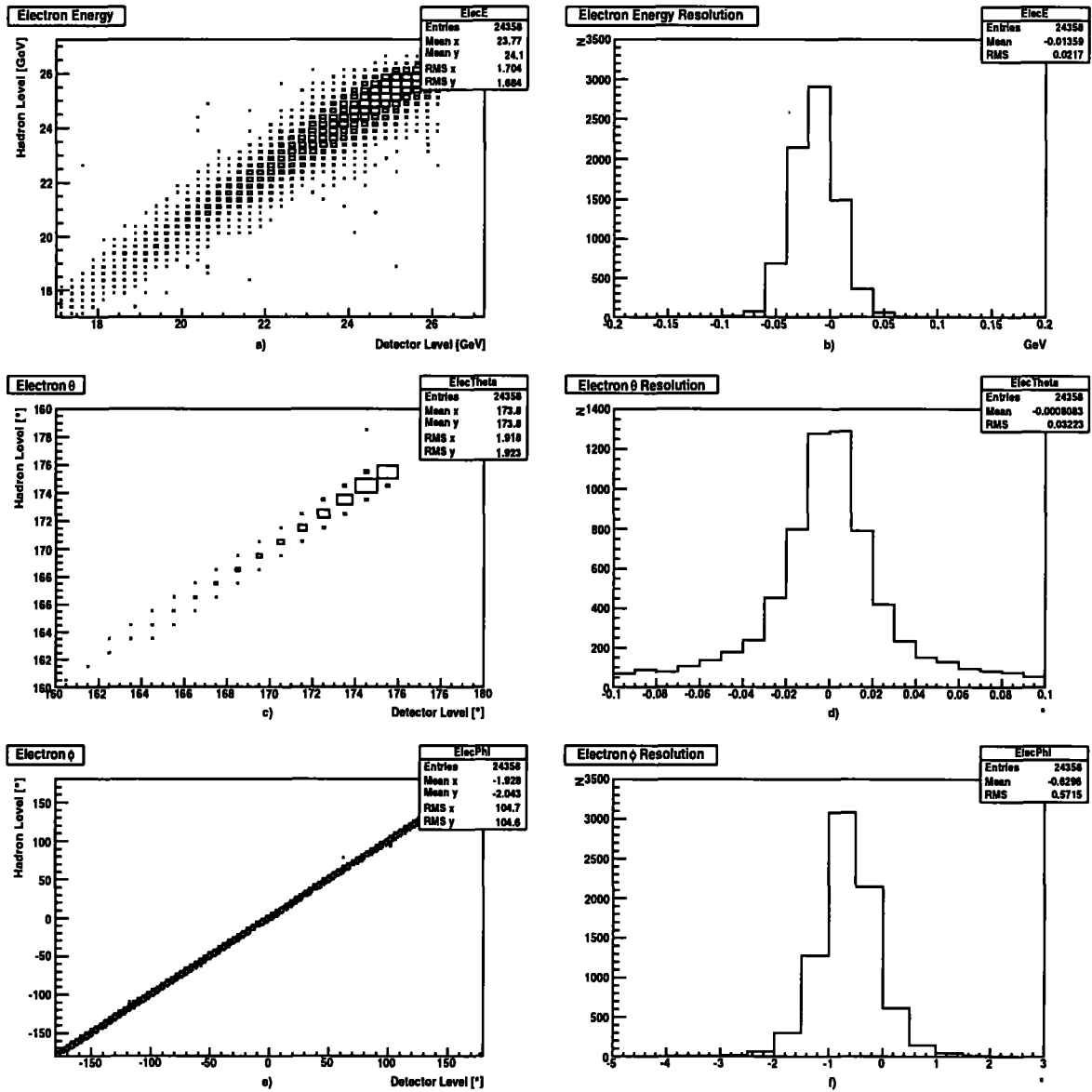
Figure 4.4: The comparison of electron energy a) and b), electron θ_{el} c) and d) and electron ϕ_{el} e) and f) on hadron and detector level

4.5 Generator Information

There exist a H1OO class "H1PartMC" which is an array with pointers to all generated particles and provides this way the information about the generated level. The Table 4.1. shows a RAPGAP output of a typical nonresonant di-pion event. It is divided to three parts. The first contains the information about the beam settings and initial conditions. The second part gives an information about the parton level and it begins with the "PDG 100" line. Then the fragmentation follows and the third part begins with the line called "string". It is the fragmentation output and it is the source for the particles that finally come to the detector simulation.

particle	type	parent	p_x	p_y	p_z	energy	mass
e+	beam	-1	0.0000	0.0000	-27.5000	27.5000	0.0000
proton	beam	-1	0.0000	0.0000	920.0000	920.0005	0.9479
Z0	doc	0	4.5032	1.0486	-1.8674	1.4538	-4.7700
e+	stable	0	-4.5032	-1.0486	-25.6326	26.0462	-0.0381
PDG 100	doc	1	0.1010	0.2497	4.2971	4.2971	-0.2700
d	doc	1	1.3535	0.5095	5.6815	5.8392	-0.5244
d	doc	5	0.6959	0.3609	4.7696	4.8336	0.0009
d	doc	2	4.8115	1.2865	2.4328	5.5429	0.0099
proton	stable	1	-0.1009	-0.2497	915.7029	915.7034	0.9662
$\bar{d}$	decayed	7	4.8115	1.2865	2.4328	5.5429	0.0099
d	decayed	1	-0.2073	0.0119	-0.0031	0.2079	0.0099
string	decayed	9	4.6042	1.2984	2.4297	5.7508	2.0699
pi+	stable	11	-0.0246	0.3601	-0.0881	0.3969	0.1396
pi-	stable	11	4.6288	0.9383	2.5177	5.3540	0.1396

Table 4.1: The illustration of a generator printout of a typical nonresonant di-pion event (All quantities are in GeV).

While looking into the generator information, one could determine which process of the pomeron exchange model is generated. This check showed, that all di-pion events used in this analysis were produced via the QPM model (Sec. 1.2.1.).
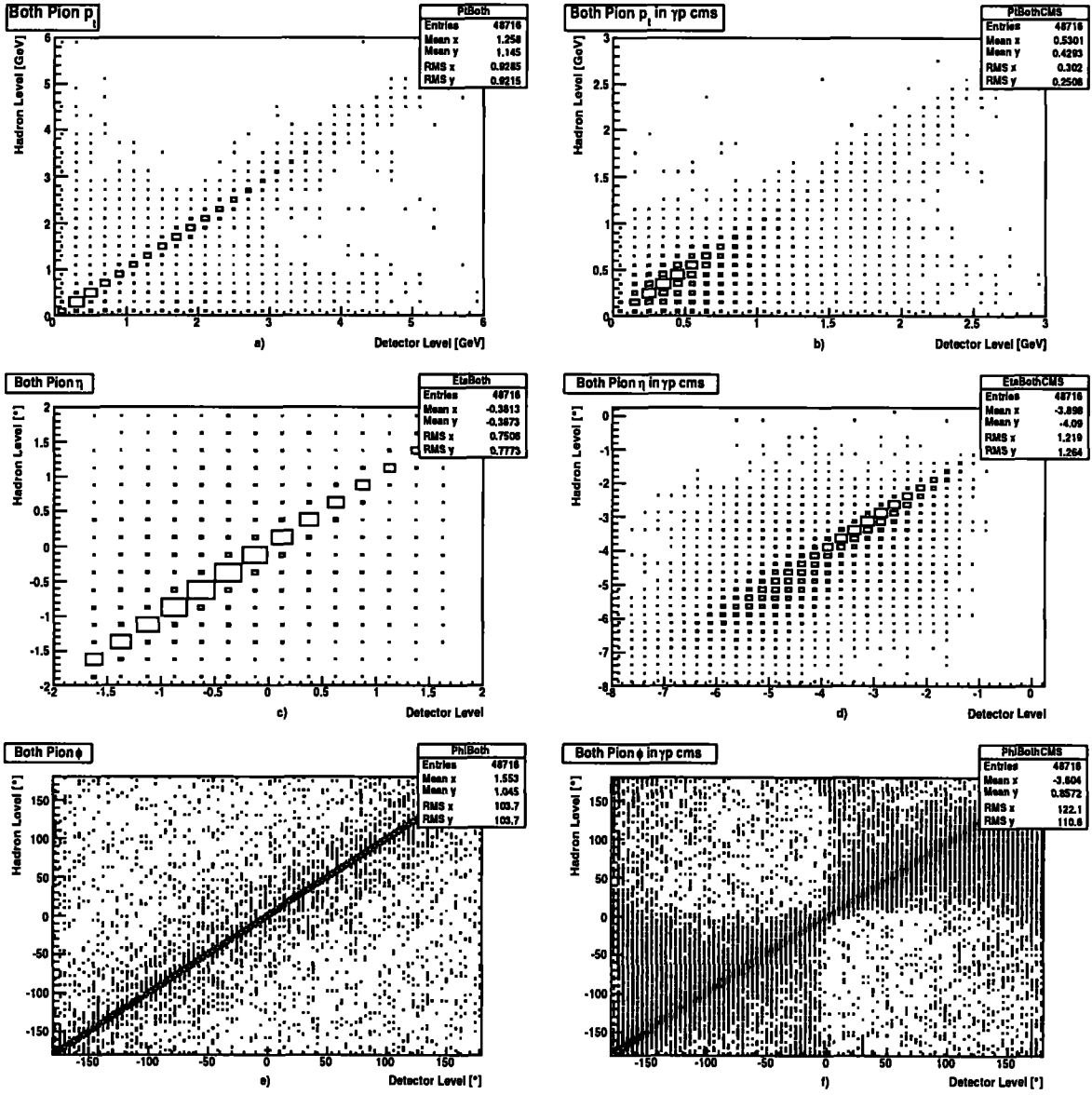
Figure 4.5: The comparison of pion characteristics in lab and γp cms on hadron and detector level. Lab frame: a) pion p_t, b) pion η, c) pion ϕ. Cms frame: d) pion p_t, e) pion η, f) pion ϕ.

4.6 The Quality of Pion Candidates Reconstruction

The Fig. 4.5. shows the correlations of basic characteristics of pion candidates. To increase statistics, both pion candidates have been put into one plot. The plots a), c) and e) show the correlation between the generated and reconstructed level in the laboratory frame. The first, third and fifth plot show the correlation of p_t, η and ϕ of pions, respectively. The plots b), d) and f) show the same variable correlations in the γp centre-of-mass frame.

The correlation of variables p_t, η and ϕ between the generated and reconstructed levels in MC is rather good in the laboratory frame. This is not the case after the Lorentz boost to the γp centre-of-mass (see Fig. 4.5. b), d) and f)). The Fig. 4.6. shows how the uniform distribution of ϕ_π in γp cms system at hadron level changes to an U-shaped ϕ_π distribution at the detector level. The variables in γp cms at detector level are strongly dependent on the Lorentz boost from lab system to γp system. If the quality of measuring of the electron is not excellent, the Lorentz boost can spoil the correlation between the detector-hadron level in γp cms system. It is also probably the reason for bad correlation on Fig. 4.5. Note that the Lorentz transformation was checked several times independently and no bug was found. The reasons of the bad correlations in γp cms system remain unclear.
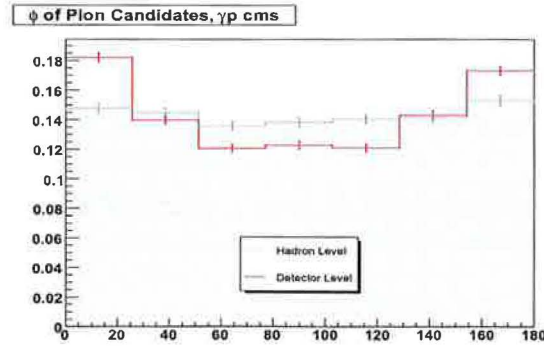

Figure 4.6: The comparison of detector and hadron level of the pion ϕ angle in the γp cms.

4.7 Monte Carlo Selection Studies of Nonresonant Di-Pions

Since there is the possibility to look into the hadron level of RAPGAP generated events, there exists a chance to improve the selection of nonresonant pions in the data sample.

Two sets of RAPGAP PEM events which satisfied all the cuts described in previous chapters have been studied. The first was the set with only two nonresonant pions and the second was all the rest. The second set is background which fakes the nonresonant di-pions at detector level (resonance decays, kaons,...). Then a study of several variables has been made in order to find some additional cuts to improve the selection. The nonresonant sample is only about 9.2% of all the selected events, therefore the histograms are normalised to unit area. If some cut could be found (i.e. some area where nonresonant di-pion events are not present and the background is), it would help to reduce the background statistics.

In the Fig. 4.7 following plots are displayed: a) the p_t of both pions in lab system, b) the pseudorapidity η of both pions in lab system, c) the $E - P_z$ variable defined in Sec. 3.1., d) the coplanarity, e) the p_t compensation and f) the sum of p_t of both pion candidates in γp cms. The coplanarity is computed as a difference of the ϕ_{el} angle of the scattered electron and of a vector that is made as a vector sum of the pion candidates. The p_t compensation is a ratio of transversal momentum of all hadrons summed in the lab frame to the p_t of the scattered electron in the lab frame. The sum of the p_t of both pion candidates in γp cms should be in an ideal case zero.

The distributions for nonresonant di-pion and background events are similar, the only exception is the transversal momentum compensation. The cut

$$P^T_{Compensation} > 0.7$$

marked by the red line in the Fig. 4.7.e) rejects effectively background events. Under this value there are almost no nonresonant di-pion events. This cut excluded 148 events from 1144 from the data sample.
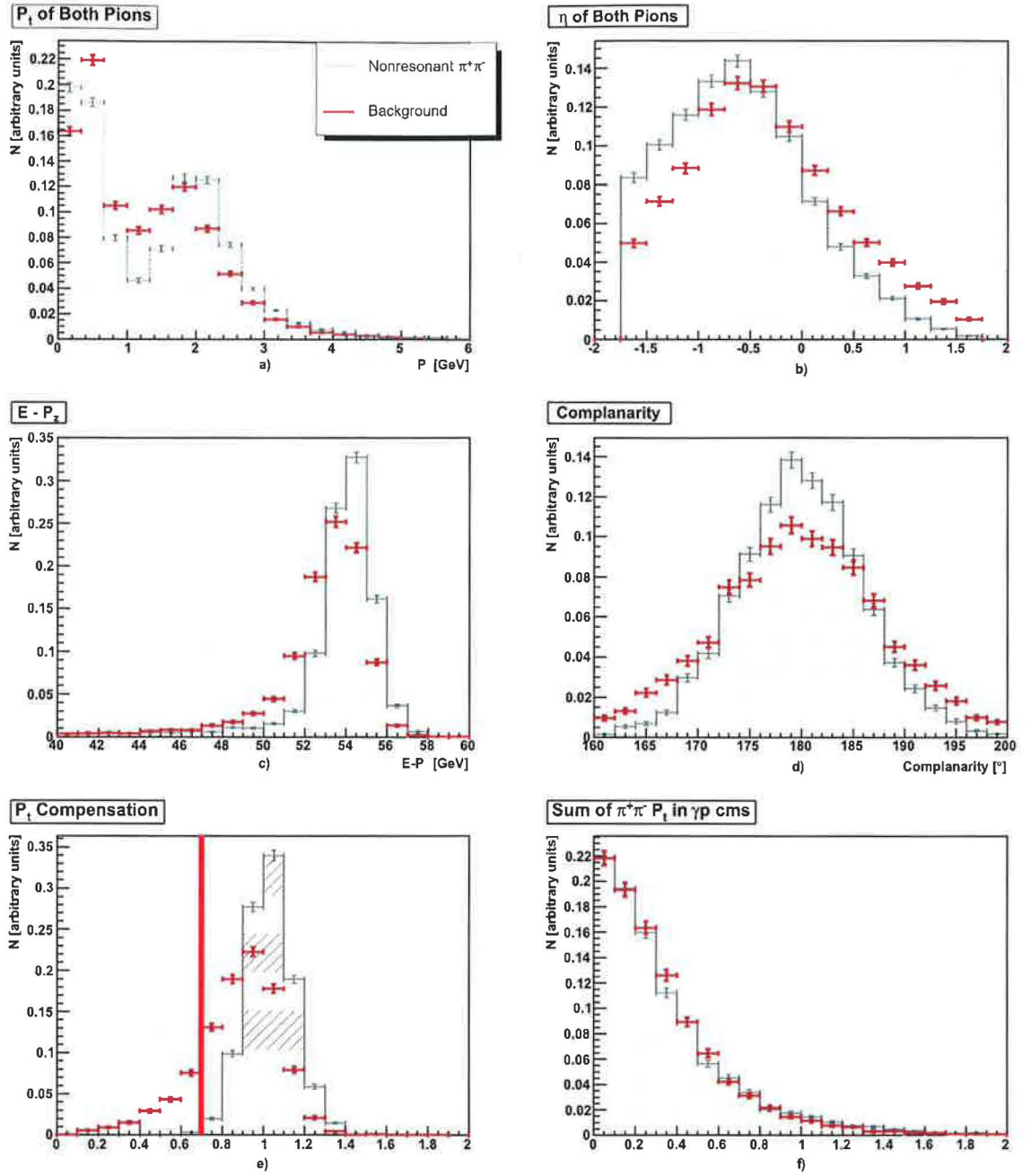
Figure 4.7: The comparison of nonresonant di-pion and background events: a) the p_t of pions, b) the pseudorapidity η of pions, c) the $E - P_z$ variable, d) the coplanarity, e) the p_t compensation and f) the sum of p_t of both pion candidates in γp cms.

Chapter 5

Comparison of Data and Monte Carlo

5.1 The Invariant Mass

5.1.1 Pomeron Exchange Model

The Fig. 5.1. shows the comparison of the $M_{\pi\pi}$ distribution for data and PEM MC. It is clear that there is a large discrepancy in the shape of data and RAPGAP MC distributions. The MC distribution has larger tail in the invariant mass region of $1.0 < M_{\pi\pi} < 3.0 \, GeV$ than observed in the data.

The invariant mass spectrum is usually fitted with the formula [26]:

$$N_{BW}\frac{1}{(m - M_\rho)^2 + \frac{\Gamma_\rho^2}{4}} + N_G e^{-\frac{(m-\mu)^2}{2\sigma^2}} + N_{Back}(m - M_{tr})^\alpha e^{-\beta m} \qquad (5.1)$$

where m is the invariant mass $M_{\pi\pi}$, N_i are the normalisation factors for each function, M_ρ is the ρ mass, Γ_ρ is the ρ decay width, μ and σ are gaussian parameters, $M_{tr} = 2M_\pi = 0.270 \, GeV$ is the threshold for the invariant mass distribution, α and β are free parameters. The first part of the equation (5.1) is the Breit-Wigner distribution describing the ρ peak. The second part - the gaussian - describes the distribution of miss-identified kaons coming from the ϕ resonance. The third part is the fit of the background.

The Fig. 5.2. presents the data (left) and Monte Carlo (right) invariant mass distributions fitted by the formula (5.1). To better understand the nonresonant tail of the MC invariant mass spectrum, one had to look to the generator information again. There are several resonances in the invariant mass region $0 < M_{\pi\pi} < 3 \, GeV$:
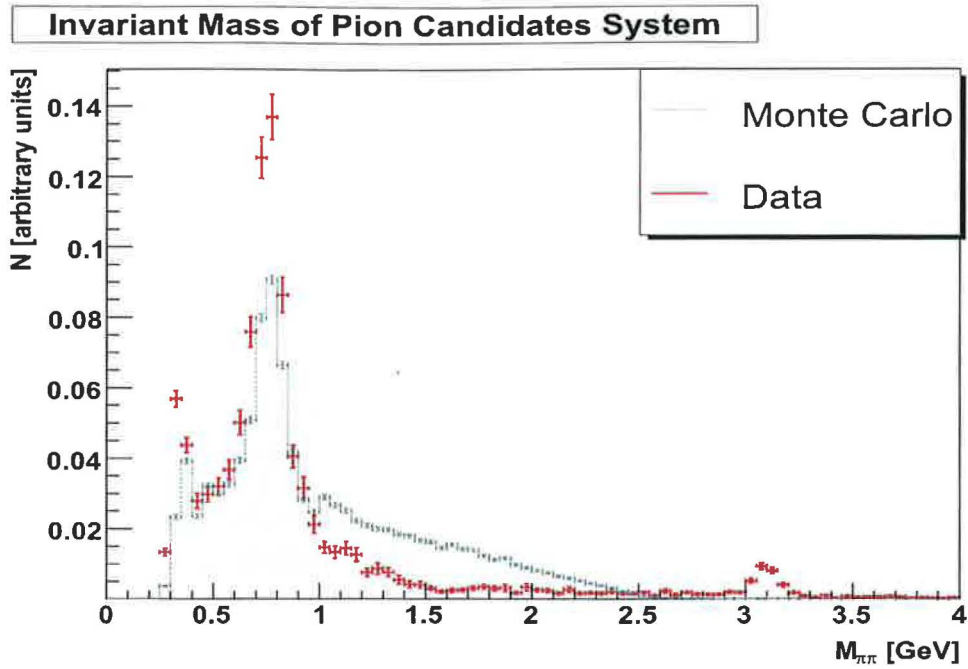
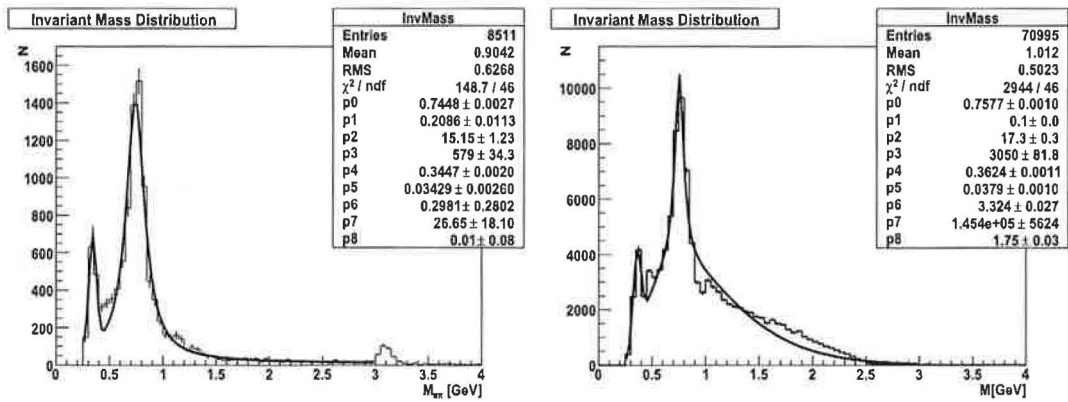Figure 5.1: The comparison of data and Monte Carlo invariant mass $M_{\pi\pi}$ distribution.

Figure 5.2: The fitted invariant mass $M_{\pi\pi}$ spectrum for data (left) and Monte Carlo (right).
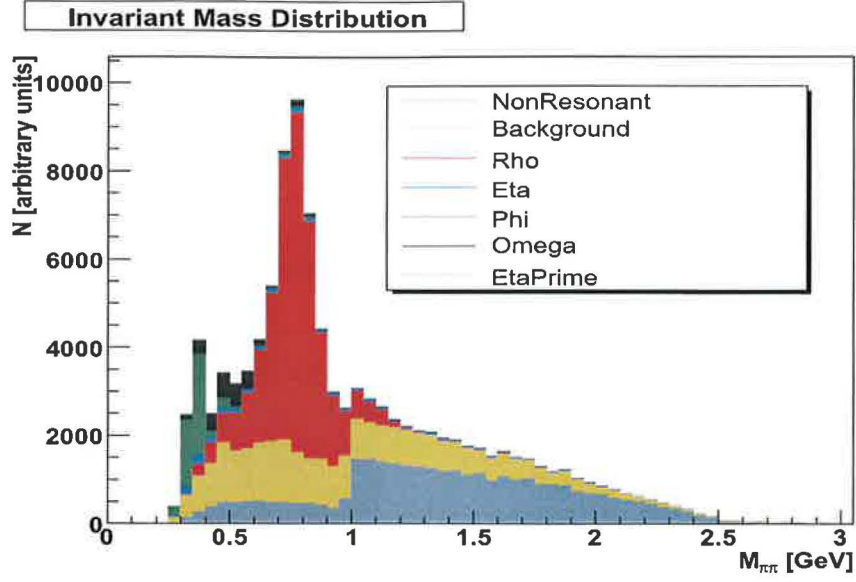
Invariant Mass Distribution

Figure 5.3: The invariant mass spectrum with emphasised contributions from different final states.

$$\rho \rightarrow \pi^+\pi^-$$
$$\omega \rightarrow \pi^+\pi^-\pi^0$$
$$\eta \rightarrow 2\gamma$$
$$\rightarrow 3\pi^0$$
$$\rightarrow \pi^0 2\gamma$$
$$\eta' \rightarrow \pi^+\pi^-\eta$$
$$\rightarrow \rho^0\gamma$$
$$\rightarrow \pi^+\pi^-\gamma$$
$$\phi \rightarrow K^+K^-$$

Table 5.1: Decays of resonances in the invariant mass range $0.27\,GeV < M_{\pi\pi} < 3.0\,GeV$
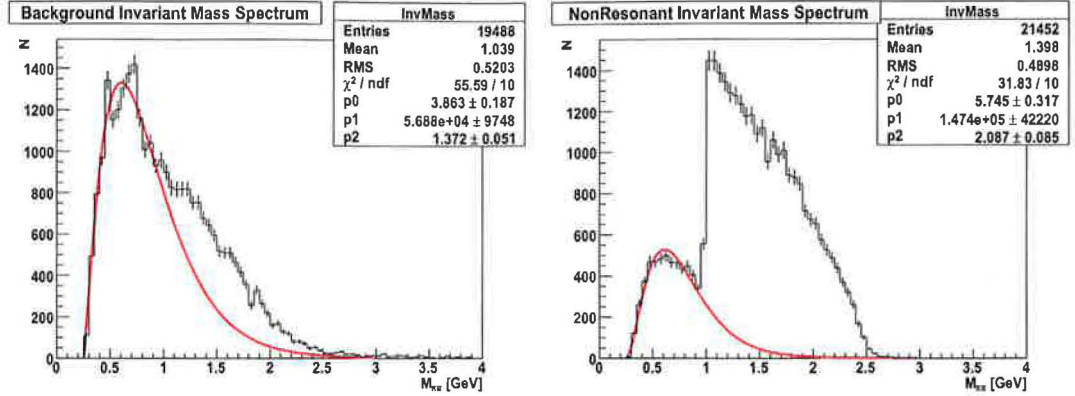
Figure 5.4: The fitted invariant mass $M_{\pi\pi}$ spectrum for the background sample (left) and for the nonresonant sample (right).

The RAPGAP MC file has been divided into samples corresponding to different generated final states - $\rho, \omega, \eta, \eta', \phi$, nonresonant $\pi^+\pi^-$ and background. The invariant mass spectrum with respect to such sorting is shown in Fig. 5.3. From the plot it is obvious that the spectrum behaves unphysically. There is a sharp edge about the value of 1.0 GeV in the nonresonant spectrum that has large impact to the whole spectrum.

The nonresonant and the background samples are the most important in the invariant mass region of interest ($1.1 < M_{\pi\pi} < 3.0~GeV$). Because of this fact, these samples have been investigated more thoroughly. The figure Fig. 5.4. shows these invariant mass spectra. To fit this samples, the background function from eq. (5.1.) has been used. The fitted parameters are following:

$$f_{nonres} = 1.474 \cdot 10^5 (m - M_{tr})^{2.087} e^{-5.745m} \qquad (5.2)$$

$$f_{back} = 5.688 \cdot 10^4 (m - M_{tr})^{1.372} e^{-3.863m} \qquad (5.3)$$

where m is the invariant mass $M_{\pi\pi}$. The red lines in Fig. 5.4 show the fitted functions. The fit was made in the range $0.27 < M_{\pi\pi} < 1.0~GeV$ and then extended to whole spectrum up to $3.0~GeV$. The parameters above has been stored and then in the analysis procedure nonresonant or background events were reweighted by these functions.

The invariant mass spectrum after the reweighting is shown in the Fig. 5.5. and the comparison with the data is in Fig. 5.6. After the reweighting, the Monte Carlo and the data are in a much better agreement than previously.
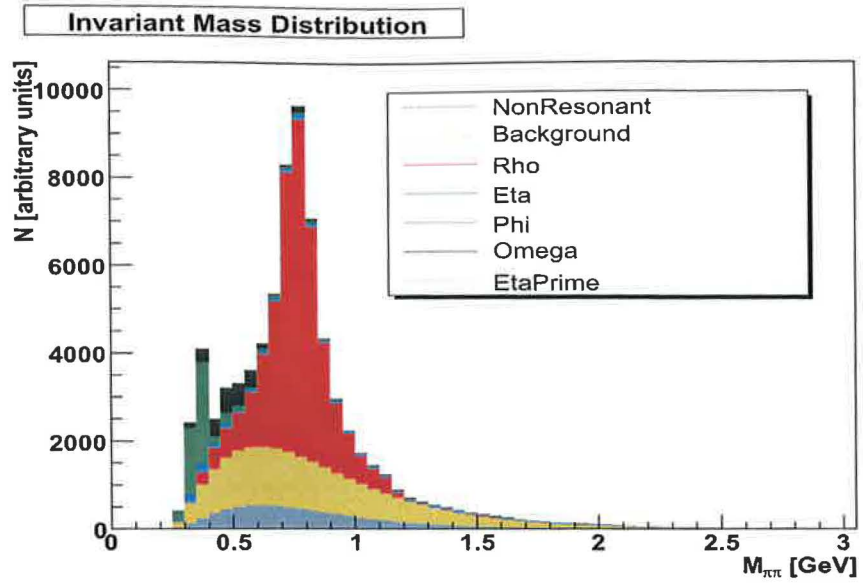
Figure 5.5: The invariant mass spectrum with emphasised contributions from different final states. The reweighting procedure has been applied.
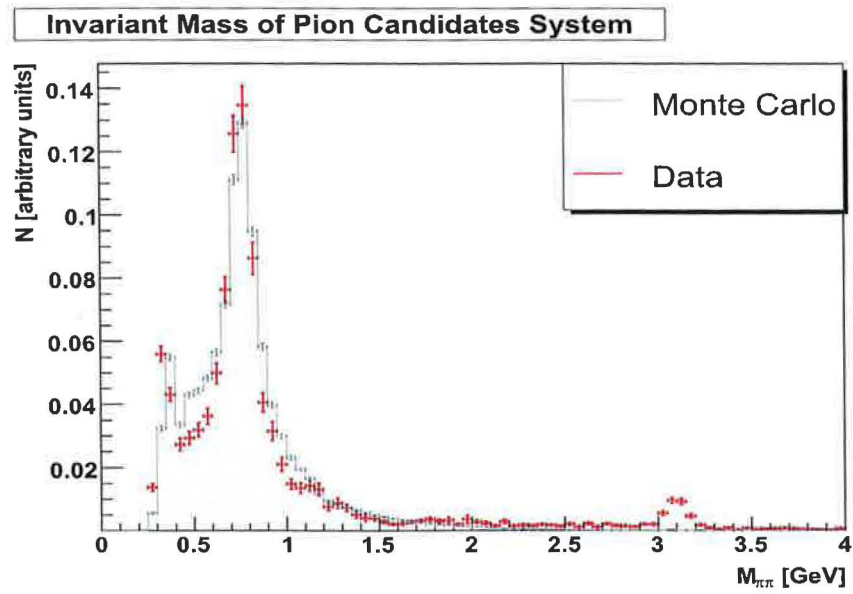

Figure 5.6: The comparison of data and Monte Carlo invariant mass $M_{\pi\pi}$ distribution after the reweighting.

5.1.2   Two Gluon Exchange Model

The Fig. 5.7. shows the invariant mass distribution of the data compared with the RAPGAP MC generated with the two gluon exchange. It is obvious that the MC spectrum does not contain any resonances as in the Sec. 5.1.1. The spectrum is flat in the whole range. The generator information has been investigated as well with the result that no resonances from Table 5.1. were found and - what is more important - no nonresonant di-pions were produced.

This facts were the reason, why the RAPGAP two gluon exchange Monte Carlo was not used in the further analysis.
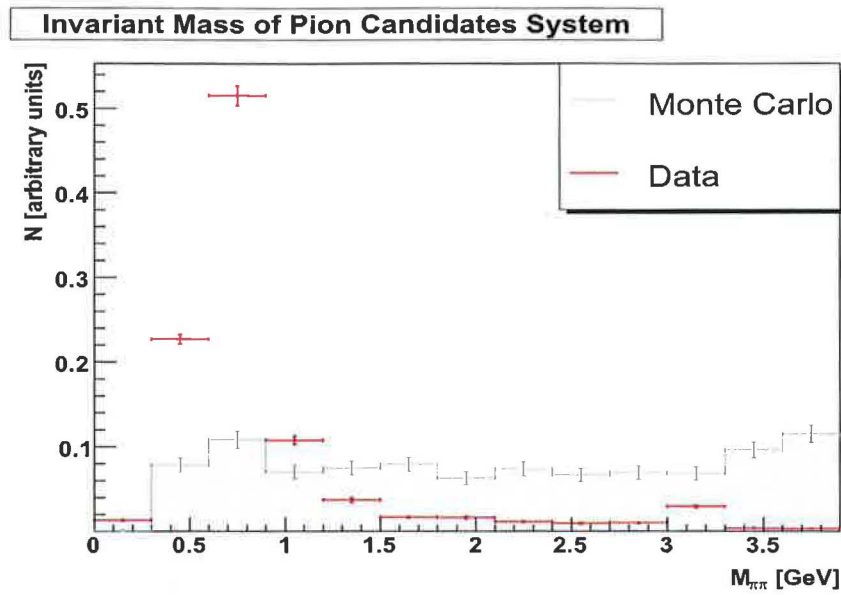

Figure 5.7: The comparison of data and RAPGAP TGE invariant mass $M_{\pi\pi}$ distribution

5.2   Results

5.2.1   General Comparison

This section provides the comparison of data and RAPGAP PEM. All cuts and reweightings described in the previous chapters have been applied. In Fig. 5.8. the z-vertex distribution for data and MC is shown. The result of usually used reweighting procedure to fit the MC to the data by the z-vertex coordinate is shown on the right plot in Fig. 5.8. All histograms were normalised to unit

area, the statistics of Monte Carlo is more than 20times higher than for the data (22,868 MC vs. 996 data events). Therefore the statistical errors for the data are significantly larger than for the MC.
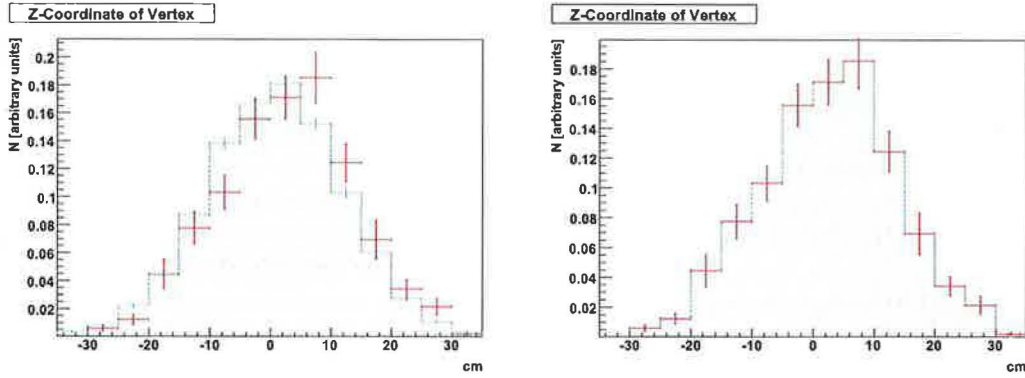

Figure 5.8: The z-coordinate of the vertex before (left) and after (right) the MC z-vertex reweighting

In the Fig. 5.9. the comparison of basic variables and the scattered electron variables is shown. The Fig. 5.9. a) shows the $E - P_z$ variable. On the b) and c) the Q^2 and y distributions are presented. The $x_{I\!P}$ distribution in Fig. d) demonstrates that the cut $x_{I\!P} < 0.04$ has been redundant. The next four histograms show the scattered electron comparison: e) the electron energy E_{el}, f) the electron θ_{el}, g) the electron ϕ_{el} and finally h) RSpaCal - radius of the scattered electron energy cluster in SpaCal measured from the beam pipe in the transversal plane $x - y$ plane.

The Fig. 5.10. compares the hadronic variables (a) and b)) and pion candidates characteristics (c)-h)). The Fig. a) shows the total hadronic energy W, Fig. b), the square of the four momentum transferred at the proton vertex t, which can be also interpreted as the square of the pomeron momentum four-vector. The statistics for the pion candidates histograms has been improved by plotting both pions into one histogram. The pion candidates histograms show various variables in laboratory and γp cms system: pion transversal momentum, pion pseudorapidity and pion azimuthal angle ϕ.

Histograms c), e) and g) present the variables in the laboratory frame, d) and f) show the pion transversal momentum and the pion pseudorapidity in the γp centre-of-mass system. The histogram 5.10. f) shows the sum of the transversal momenta of the pions (vector sum) in the γp system.

The Fig. 5.11 shows the p_t compensation plot (a)) and the coplanarity (b)).
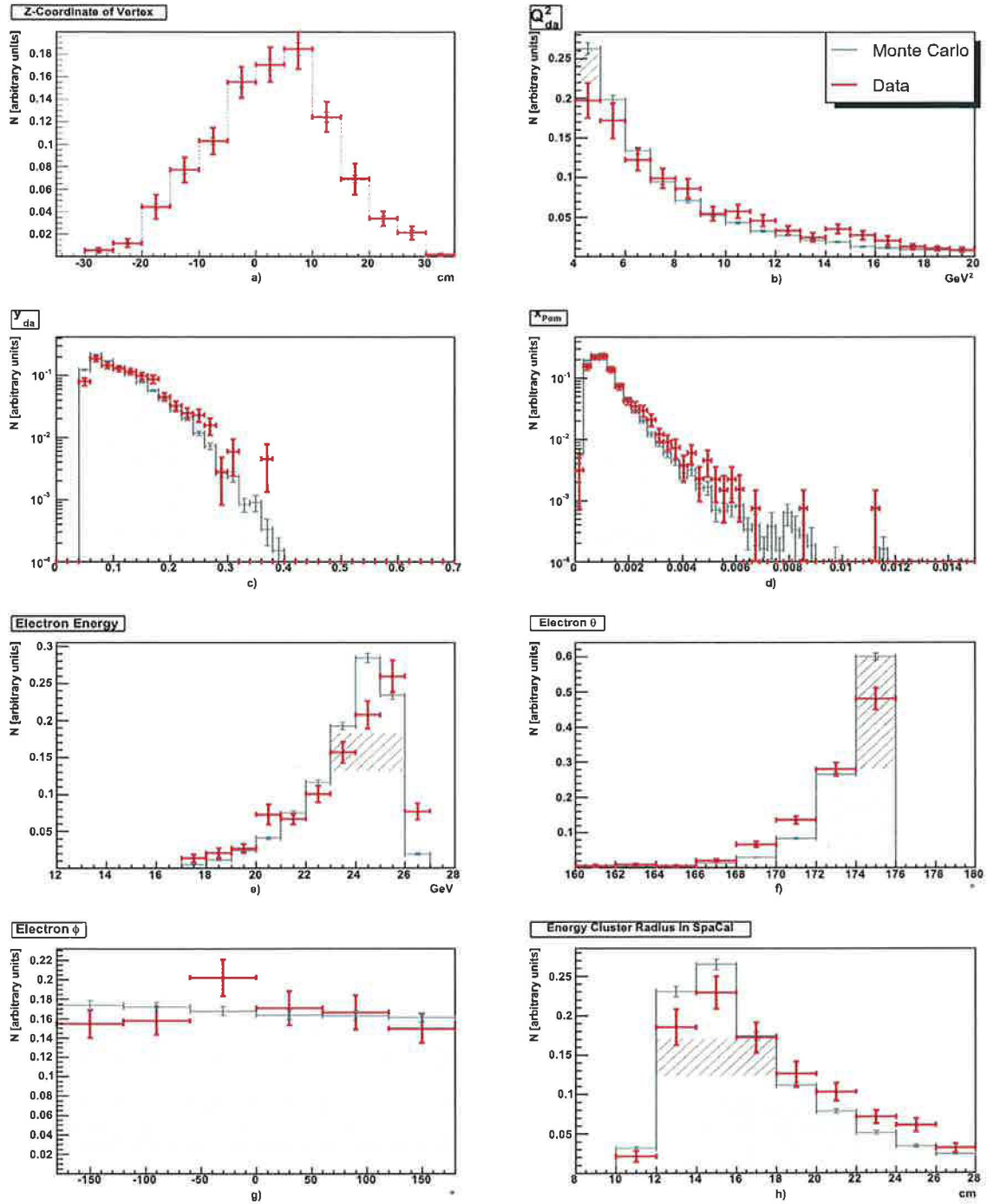
56

Figure 5.9: The comparison of data and Monte Carlo: a) $E - P_z$, b) Q^2, c) y and d) $x_{I\!P}$ distribution, e) the electron energy E_{el}, f) the electron θ_{el}, g) the electron ϕ_{el} and h) RSpaCal - the radius of the scattered electron energy cluster in SpaCal.
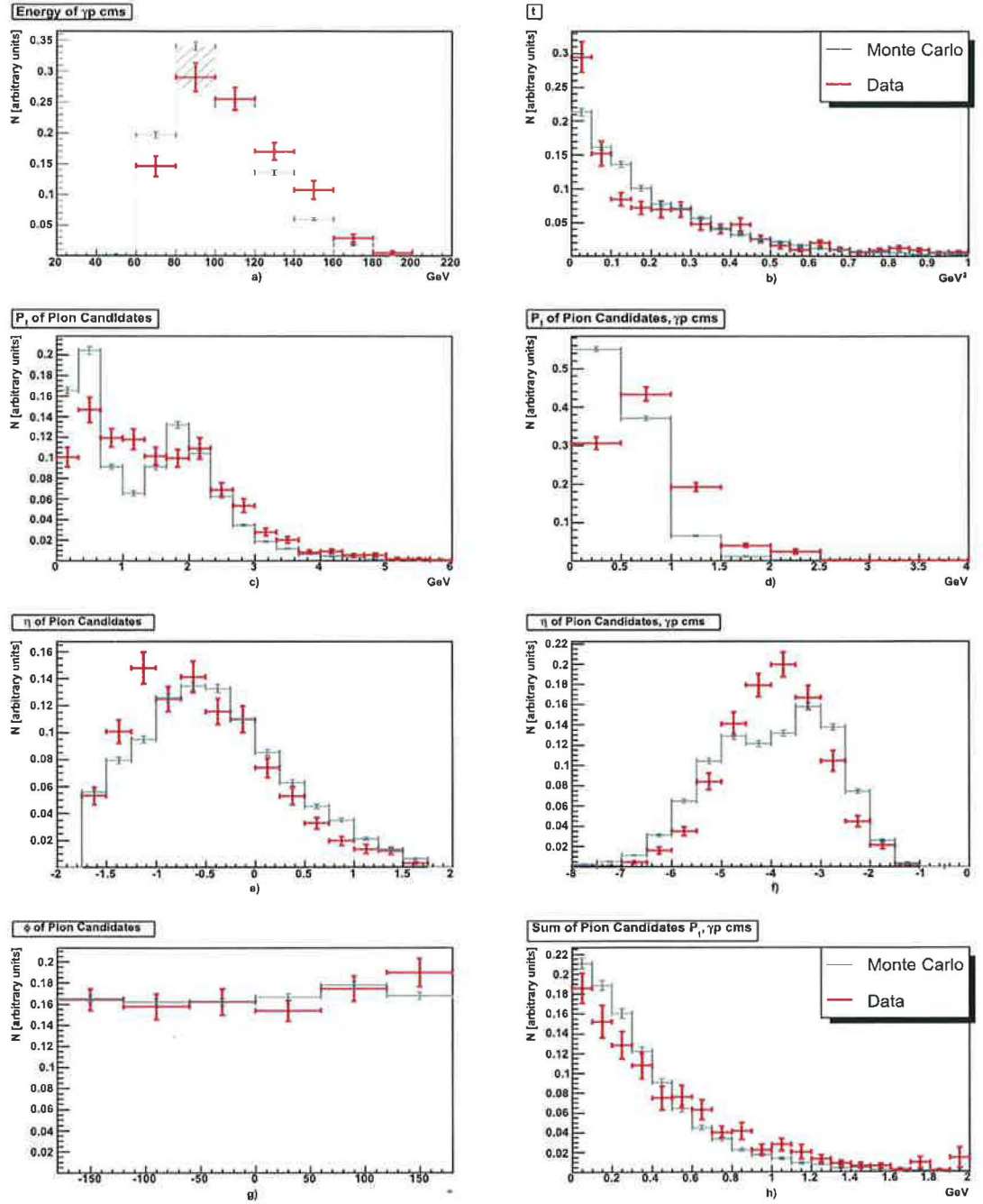
Figure 5.10: The comparison of data and Monte Carlo: a) total hadronic energy W, b) t, the square of the four momentum transferred at the proton vertex, c) pion transversal momentum in lab, d) pion transversal momentum in cms, e) pion pseudorapidity η in lab, f) pion pseudorapidity η in γp cms, g) pion ϕ in lab and f) sum of the transversal momenta of the pions in γp cms.
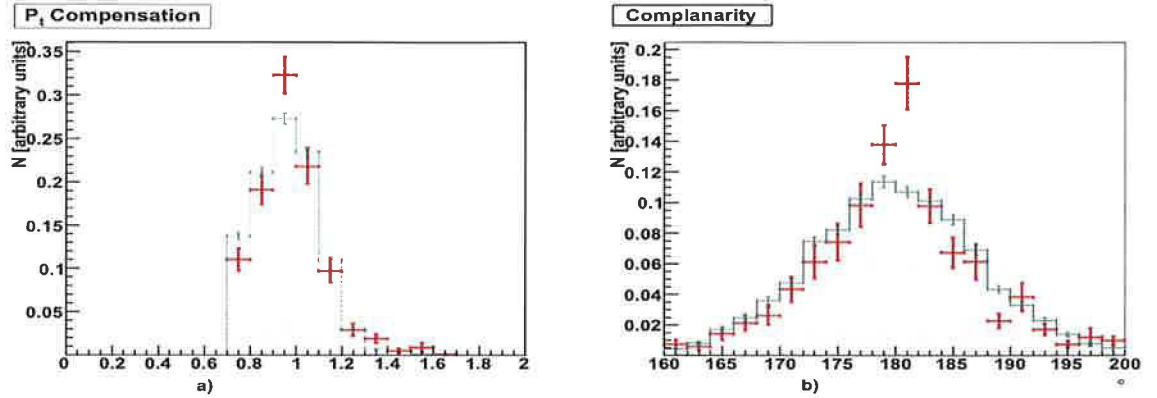
58

Figure 5.11: The comparison of data and Monte Carlo: a) the p_t compensation in lab, b) the coplanarity in lab.

It is seen that data and RAPGAP PEM agree within errors rather well for global characteristics of the event with exception of the scattered electron energy E_{el} and the $E - P_z$ distribution. The description of data by MC for pion characteristics is much poorer, mainly in the γp cms system.

5.2.2   Azimuthal Distribution

The distributions of the azimuthal angle ϕ for both pion candidates for data and RAPGAP PEM are presented in Fig. 5.12. The ϕ distribution of the data is within statistical errors close to uniform, while MC shows the U-like dependence. Note that this U-shape distribution in MC was found to be the result of the Lorentz transformation from lab to γp cms system (as discussed in Sec. 4.6. in Fig. 4.6.) at the detector level. It seems that this effect is not present in the data.

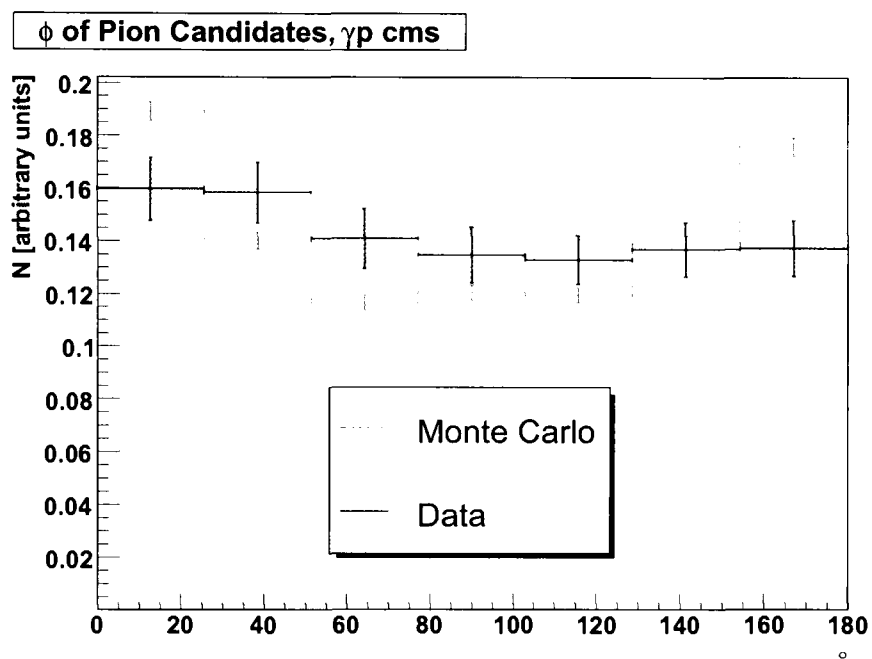RAPGAP PEM Monte Carlo is definitely not able to describe the ϕ distribution for di-pion nonresonant events.

Figure 5.12: The comparison of data and MC of the ϕ distribution in the γp cms.

60

Chapter 6

Conclusion and Summary

The analysis of the data from 1999/2000 has been accomplished. The DIS subtrigger element s61 efficiency has been checked for the data and the scattered electron has been selected. Two nonresonant pions have been chosen and diffraction cuts were applied. The invariant mass spectrum $M_{\pi\pi}$ has been investigated and the cut on $1.1 < M_{\pi\pi} < 3.0\ GeV$ has been used.

The aim of this analysis was to compare the azimuthal ϕ distribution in the γp centre-of-mass system in di-pion nonresonant events with two model predictions. These were represented here by two versions of RAPGAP 2.08 - RAPGAP resolved pomeron exchange and RAPGAP two gluon exchange. It was found that the RAPGAP TGE does not contain any nonresonant di-pion final states.

The precision of the Q^2 and y methods as well as the precision of the electron and pion reconstruction has been determined. The generator information of the RAPGAP PEM Monte Carlo was used to compare a sample with nonresonant di-pions with an other sample with the background. This comparison led to the improvement of the data selection.

The RAPGAP PEM Monte Carlo has been reweighted to obtain better agreement of spectrum of effective di-pion mass and then compared with the data. The agreement of MC with data is however rather poor. The azimuthal distribution ϕ of di-pion events in data is flat, while in MC we obtained an U-like shape. It is evident that both versions of RAPGAP Monte Carlo are not suited for this type of analysis.

Note e.g. that in the analysis [22] a special Monte Carlo based on MC ZEUSVM was developed for a similar kind of analysis.

Bibliography

[1] G. Wolf, *HERAPhysics*, DESY preprint 94-022 (1994).

[2] J.I.Friedman.
Deep inelastic scattering : Comparisons with the quark model. Rev. Mod. Phys. 63 (1991) 615-627.

[3] Bartel et al. *The transverse and longitudinal cross sections for electroproduction of pions near the $\Delta(1236) - isobar$*. Phys. Lett. B 27(1968)660-662.

[4] M. Breidenbach et al. *Observed behaviour of highly inelastic electron − proton scattering*. Phys. Rev Lett. 23 (1969) 935-939.

[5] R.P.Feynman *Photon − Hadron Interactions*. Benjamin, 1972.

[6] G. Altarelli and G. Parisi, *Asympatotic freedom in parton language*. Nucl. Phys. B 126(1977) 298-318.

[7] H1 Collaboration, *Observation of hard processes in rapidity gap events in γp interactions at HERA*. Phys. Lett. B 346 (1995) 399-414.

[8] H1 Collaboration, *Deep inelastic scattering events with a large rapidity gap at HERA*. Nucl. Phys. B 429 91994) 477-502.

[9] P. D. B. Collins and A. D. Martin, *Hadron Interactions*. Adam Hilger Ltd, 1984

[10] I. I. Pomeranchuk. *Equality of the nucleon and antinucleon total interaction cross section at high energies*. Sov. Phys JETP 7 (1958)499-501.

[11] A. Donnachie and P. V. Landshoff, *Total cross sections*. Phys. Lett. B 296 (1992) 227-232.

[12] WA91 Collaboration, *Observation of a narrow scallar meson at 1450 MeV in the reaction $pp \to p_f(\pi^+\pi^-\pi^+\pi^-)p_s$ using the CERN Omega Spectrometer*. Phys Lett. B 324 (1994) 509-514.

[13] WA102 Collaboration, *A kinematical selection of glueball candidates in central production*. Phys Lett. B 397 (1997) 339-344.

[14] G. Ingelman and P. Schlein, *Jet structure in high mass diffractive scattering*. Phys. Lett. B 152 (1985) 256-260.

[15] UA8 Collaboration, *Evidence for a super − hard pomeron structure*. Phys. Lett. B 297 (1992) 417-424.

[16] H1 Collaboration, *First measurement of the deep − inelastic structure of proton diffraction*. Phys. Lett. B 348 (1995) 681-696.

[17] H1 Collaboration, *A measurement and QCD analysis of the diffractive structure function $F_2^{D(3)}$*. Paper pa02-061 contributed to the 28th International Conference on High Energy Physics, Warsaw, Poland, July 1996.

[18] Y. Y. Balitskii and L. N. Lipatov, *The Pomeranchuk singularity in quantum chromodynamics*. Sov. J. Nucl. Phys. 28 (1978) 822-829.

[19] H. Jung, private communication, 2005/06.

[20] J. Bartels, C. Ewerz, H. Lotter, M. Wuesthoff, M. Diehl, *Quark − Antiquark Jets in DIS Diffractive Dissociation*,hep-ph/9609239.

[21] J.Bartels, C.Ewerz, H.Lotter, M.Wuesthoff, *Azimuthal Distribution of Quark − Antiquark Jets in DIS Diffractive Dissociation*,hep-ph/9605356.

[22] ZEUS Collaboration, *Studies of the hadronic component of the photon light − cone wave function using exclusive di − pion events at HERA*, ZEUS-prel-04-035.

[23] D. Šálek, *Study of di − jet production in diffractive ep interactions*, diploma thesis, Prague, 2006

[24] C. Gwilliam, X. Janssen, online reference at: *https : //www − h1.desy.de/icas/oop/roothtml/current/src/H1PartLightVMDiff.cxx.html*

[25] H1 Central Trigger Home Page, *http : //www − h1.desy.de/trigger/*

[26] X. Janssen, private communication, 2005/06.

[27] H. Jung, *Monte Carlo implementation of diffraction at HERA*, hep-ph/9809374v1.

[28] H1 Collaboration, *Multiplicity structure of inclusive and diffractive deep inelastic e^+p collisions at HERA*, H1 prelim-05-015.

[29] Particle Physics Booklet, july 2004, available at: $http://pdg.lbl.gov/$